

Global concurrent cross-scale nonlinear analysis approach of complex CFRD systems considering dynamic impervious panel-rockfill material-foundation interactions



Kai Chen^{a,b}, Degao Zou^{a,b,*}, Xianjing Kong^{a,b}, Yang Zhou^{a,b}

^a The State Key Laboratory of Coastal and Offshore Engineering, Dalian University of Technology, Dalian, Liaoning 116024, China

^b School of Hydraulic Engineering, Dalian University of Technology, Dalian, Liaoning 116024, China

ARTICLE INFO

Keywords:

Scaled boundary polyhedron finite element method
Concurrent Cross-scale modelling
Elasto-plastic analysis
Complex geotechnical structures
Mega projects

ABSTRACT

Evaluating the seismic security of enormous structures is extremely vital, and this concern has continually motivated the trends of refined numerical simulations for years. However, the ability to perform a concurrent global refinement analysis of large-scale projects with complex spatial geometries and spanning huge scales has remained a formidable challenge in settings such as high concrete-faced rockfill dams. In this paper, a global concurrent cross-scale nonlinear analysis approach (GCCNA) benefitting from an efficient hybrid octree-based discretization technique is presented. Significantly, a polygon interface is constructed to automatically connect the cross-scale element and solve the interactions between the concrete-faced rockfill and foundation. A viscoelasticity polygonal artificial boundary element is subsequently developed to render the influence of radiation damping on an infinite foundation so that the travelling wave effect on the dynamic response and stabilization can be captured. A high-efficiency and economically time-consuming solution strategy is adopted, wherein the scaled boundary finite element is introduced to manage the minority polyhedrons in the generated octree model, and the numerous hexahedrons are assigned to the isoparametric element. The features of rapid discretization, high flexibility, extraordinary grid reconstruction and coupling with the conventional finite element are contained perfectly, which are demonstrated via the comprehensive elasto-plastic dynamic simulation of an extremely complicated practical constructed highest rockfill dam. The proposed approach has attractive potential and practicability for the efficient refinement analysis of complicated enormous engineering structures and can be readily extended to subterranean structures, nuclear plants, and architectural and aviation structures.

1. Introduction

Over the past decades, great changes have occurred around the world, and the most impressive achievements might have occurred in China. The large-scale projects constantly emerging from China, such as skyscrapers, oversize bridges, metro projects, and extremely high dams, have attracted global attention.

China is an earthquake-prone country that is located in the earthquake belt along the western region of the Pacific Ocean, thus making seismic safety assessments of prime importance for these large-scale projects. These assessments are especially important for high rockfill dams located in meizoseismal areas, where the consequences of an earthquake would be extremely frightening and induce serious secondary disasters to downstream cities following dam failure. Therefore, it is of great theoretical practical significance to evaluate the safety of these huge structures. In this paper, the meticulous simulation of a high

dam is used as an example of a representative application of this approach to large-scale projects.

Many high earth-rockfill dams have been constructed or planned in the western region of China. More recently, the heights of these constructed or designed dams have increased to 300 m from 200 m; a statistical illustration of this change is shown in Fig. 1-1, and plentiful technical problems arise spontaneously with this change in height. For instance, the acceleration of an earthquake becomes stronger, and the geological conditions become more complex. In addition, the concept and method of high dam design used are basically the same as those that have been used since the middle of the last century. It is difficult to adapt to the rapid development of high dam construction practices (thus far, there is no design specification for high dams above 200 m), which is a prominent issue in the field of seismic safety.

Finite element numerical simulations play a crucial role in the safety assessment of reservoirs with high dams. From the perspective of

* Corresponding author at: The State Key Laboratory of Coastal and Offshore Engineering, Dalian University of Technology, Dalian, Liaoning 116024, China.
E-mail address: zoudegao@dlut.edu.cn (D. Zou).

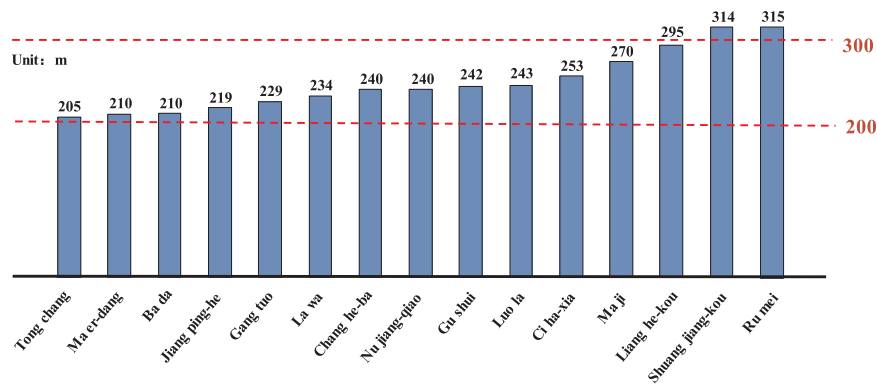


Fig. 1–1. The height statistics of typical constructed and planned high earth-rockfill dams.

variable element size, the current formulation of the numerical methods tends to require refined element discretization when approaching an analytical solution. In other words, the smaller the cell size discretizes, the higher the accuracy that can be obtained. Using a full-scale global refinement analysis is strongly recommended when investigating the damage evolution of an impervious body, assessing progressive failure processes and evaluating the ultimate seismic capacity. However, the conventional burdensome mesh generation/regeneration [1,2] and expensive computational costs of solving these complicated elasto-plastic problems often severely hamper the practical applications of this method in engineering. More efforts should be devoted to develop a highly efficient refinement meshing strategy and matched analysis approach.

Significant advances in the modelling of earth-rockfill dams have occurred in the past several decades. Syed Khalid [3] conducted an early nonlinear analysis. Then, three-dimensional finite element analysis was carried out with the development of a computer model [4]. Recently, Kong, Zou and their team developed a systematic analysis method for this kind of project, including a generalized plasticity model for coarse-grained soils [5], large-scale shaking table model tests [6], simulations of practical engineering [7,8], and dynamic damage evolution [9].

However, as many factors are considered and the current numerical simulations are based on uniform grids (mainly tetrahedrons and hexahedrons), the large amounts of time needed for model building and computational time are untenable. To circumvent this problem, Xu [9] carried out a refined damage study using a non-uniform mesh to model the 2D damage evolution of a concrete face. Qu [10] explored a plane interface element with asymmetric nodes to alleviate the degree of modelling difficulty. It is an undeniable fact that there are still challenges associated with efficiently generating a 3D mesh and a matching analysis method for high rockfill dams.

Octree grids possess the advantages of robust mesh adaptation, fast reconstruction and straightforward data access due to their simple Cartesian structure and embedded hierarchy [11]. The numerical computing community has become increasingly reliant on this method, which has been employed in fields including computational fluid dynamics and plasma physics [11–14]. However, no studies have used the octree-based adaptive grid technique to simulate the elasto-plastic responses of high earth-rockfill dams. The goal of this study is to contribute results that fill this void.

However, the Cartesian structures of octree meshes require a special technique for handling the extra hanging nodes on partial edges since the unstructured grid itself generates the inharmonious displacement illustrated in Fig. 1–2. The multi-point-constraint subroutine [15] integrated into ABAQUS, as well as the flexible polyhedron element method [16], can be introduced to eliminate this defect. An alternative solution, which is called the scaled boundary finite element method and is readily formulated for polyhedron elements, is highly recommended

to solve these so-called unstructured grids. This method is semi-analytical and was first proposed by Wolf and Song [17]; it has inherited the advantages of the boundary element method (BEM) [18,19] and the finite element method (FEM). The Scaled Boundary Finite Element Method (SBFEM) has reached a level of maturity in numerical simulations, as evidenced by its application in electromagnetic problems [20,21], elasto-plastic analysis [22–24], crack propagation problems [25–28], layered soil and soil-structure interactions [29,30], 3D steady-state heat conduction [31], sloshing analysis of liquid storage tanks [32], analysis of dynamic interactions of CFRD-compressible reservoir system [33], wave interaction and propagation simulations [34–36], heat conduction problems [37], seismic problems [38,39], nonlinear dynamic analysis of saturated soil [40], and rapid automatic image-based stress analysis [41,42].

In this paper, we propose a Global Concurrent Cross-scale Nonlinear Analysis (GCCNA) method, combined with the octree-based high-efficiency mesh discretization and a flexible scaled boundary polyhedron finite element, to better investigate the loading reactions of high rockfill dams. The enhanced SBPFEM technique is used, which has previously been presented by the author and reported in the literature [43]. A coupling calculation strategy is also employed, wherein the conventional finite element method is adopted to deal with standard elements (i.e., tetrahedron, pentahedron, triangular prism and hexahedron elements) and the remaining unstructured grids are assigned to the SBPFEM.

Furthermore, in geotechnical engineering simulations, interface elements are versatile tools that are widely used in capturing the relative displacements between soils and structures. Therefore, the possibility of using an arbitrary polygon interface element to automatically match with the unstructured meshes and enhance the convenience of modelling is explored. When all of the aforementioned preparation has been completed, an efficient cross-scale analysis platform for high rockfill dams can be established; this method represents a significance reference for other geotechnical engineering computation applications.

The remainder of this paper is organized as follows. First, Section 2 presents a detailed description of the intractable problems associated with the cross-scale calculations of high rockfill dams. Then, the adaptive octree-based mesh solution is provided in Section 3, and a concise SBPFEM method for polyhedron derivation is given in Section 4. The formulations and verification of the polygon interface element are also presented in Section 4. The reliability and practicability of the procedure are demonstrated in Section 5. Finally, remarks and conclusions are stated in Section 6.

2. Problems suffered from the cross-scale simulations of high rockfill dams

The content required for the cross-scale analysis of a high rockfill dam is comprehensive, including the interactions between the dam, foundation and reservoir systems; establishing an elasto-plastic theory

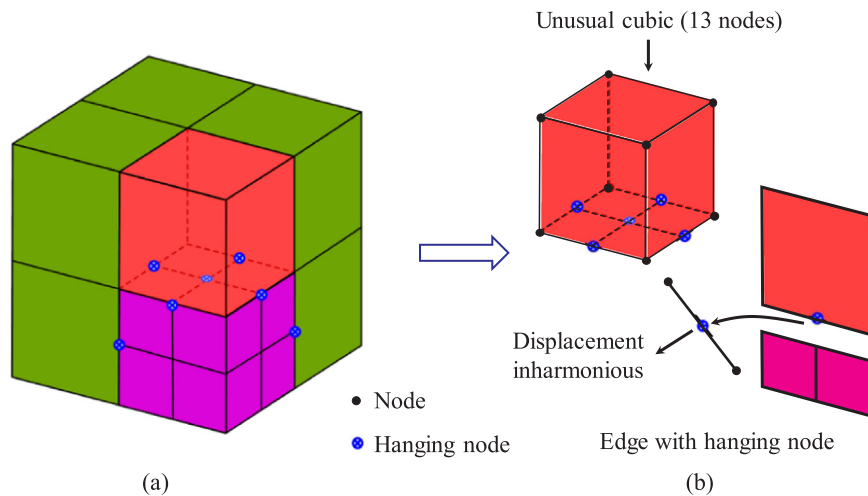


Fig. 1-2. Explanatory graph of the typical structure of octree grids.

and material constitutive model; simulating the discontinuous contacts between the soil and structures; and assessing the damage evolution and progressive failure of the anti-seepage system. One of the most substantial restrictions is developing an efficient cross-scale modelling technique and matching numerical method; the goal of this study is to mitigate this predicament.

2.1. Multiple constraints

A rockfill dam system is so complicated that multiple restricting factors need to be considered simultaneously, resulting in arduous problems associated with discretizing the model. These restrictions are carefully described as follows.

2.1.1. Partitioning of dam materials

A typical sectional drawing from the entire model is shown in Fig. 2-1, which exhibits the material distribution of a high concrete-faced rockfill dam (CFRD). The dam is divided into seven domains consisting of different materials. The major trapezoid-like structure is built on rock using rockfill I and II. The most important component, the face slab, lies on the upstream slope; its thickness T linearly varies from the dam crest to the bottom in order to withstand the invasion of changed water pressure. The toe slab is placed on the high toe wall and connects with the bottom of the face slab in order to restrain it from sliding.

2.1.2. Layered filling

A horizontally stratified rolling rockfill strategy is used in dam

construction. In order to reasonably simulate this process, layered mesh discretization is employed to approximate this layered structure. Then, the construction sequence is modeled by controlling the birth and death of elements, thus defining many boundaries that must be previously determined. A basic schematic illustration is depicted in Fig. 2-2.

2.1.3. Complex river valley

Generally, the geography of a dam site is extremely complicated. An accidental valley of a high concrete-faced rockfill dam is shown in Fig. 2-3. It would be an arduous task to discretize this geography using the traditional mesh production technology reported in the literature.

3. Adaptive octree-based solution

The conventional octree model is an efficient representation tool for three-dimensional objects. This modelling technique has generally been used for the applications of complex object representation, image processing, and robotics navigation, among others. The primary advantages of the octree-based mesh are its ability to represent complex objects with simple cubic cells. The octree model's spatial sorting property allows for efficient model updating because the size and location of any octant can be retrieved directly from the octree's hierarchical data structure. Moreover, it is straightforward to use this model for computation and applications due to its recursive subdivision strategies. A diagram is provided in Fig. 3-1.

Continuous efforts have been made to remedy the aforementioned 3D modelling difficulties. Here, we attempt to research a high CFRD

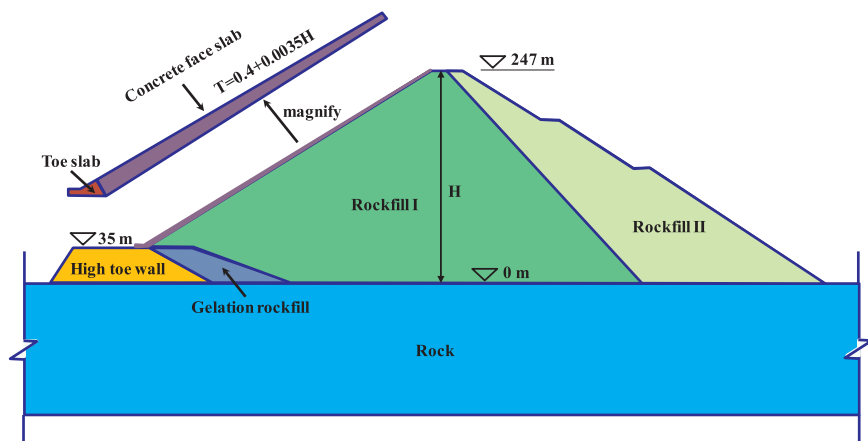


Fig. 2-1. Material distribution of a high rockfill dam.

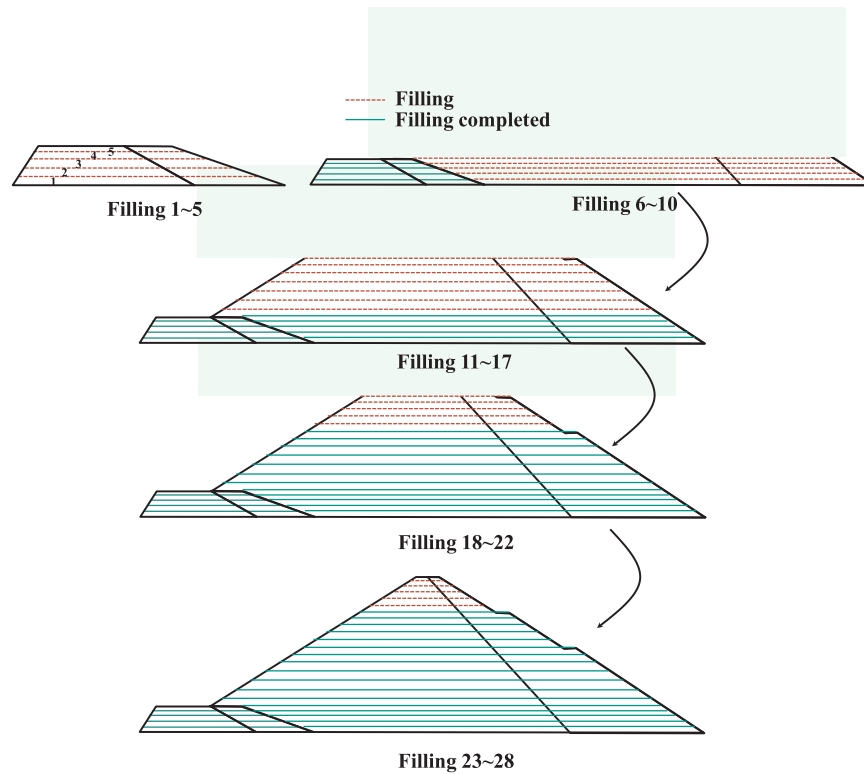


Fig. 2–2. Decomposition of horizontal filling construction.

using octree-based discretization to alleviate these problems.

3.1. Preparation

Building a stereoscopic model for CFRD is an important step before mesh generation. This step can be easily carried out using Computer-Aided Design (CAD) or Computer-Aided Engineering (CAE). Generally, this process can be summarized as follows:

(1) This first step is achieved due to the coordinated cooperation of multidisciplinary approaches. A representative design section, containing the geometric outlines and boundaries that differentiate materials, which can be embodied in Computer-Aided Design (CAD)

systems, is displayed in Fig. 3-2(a).

(2) A thalweg can subsequently be extracted from each design section of interest from the dam; it then needs to be translated into an analysis-suitable spatial curved surface for volume model production and its use in mesh generation. Fig. 3-2(b) presents the complex valley surface and a cuboid including dam material information, which is discussed in Fig. 2-1.

(3) By overlaying the valley surface and volume and executing a Boolean operation, the final volume model for mesh discretization is readily obtained, as illustrated in Fig. 3-2(c). This is a simple task and only takes a small amount of time relative to the overall analysis process.

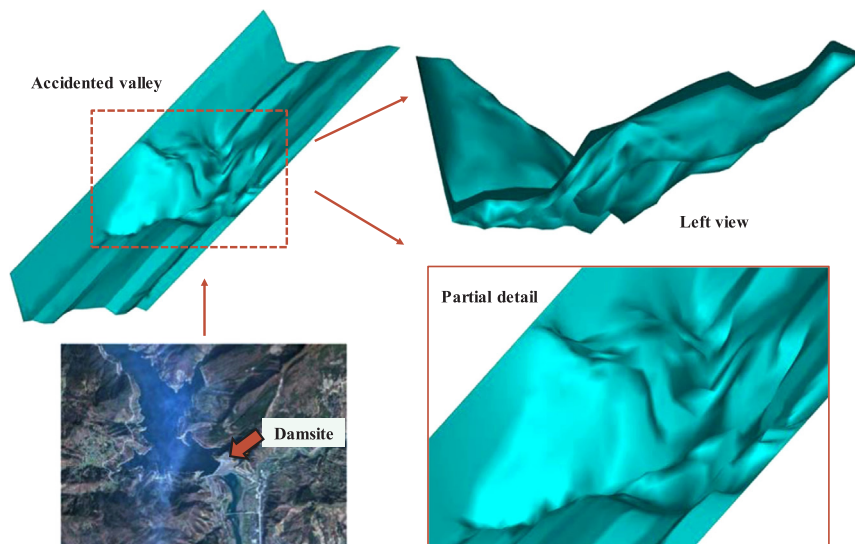


Fig. 2–3. Complex accidental valley surface.

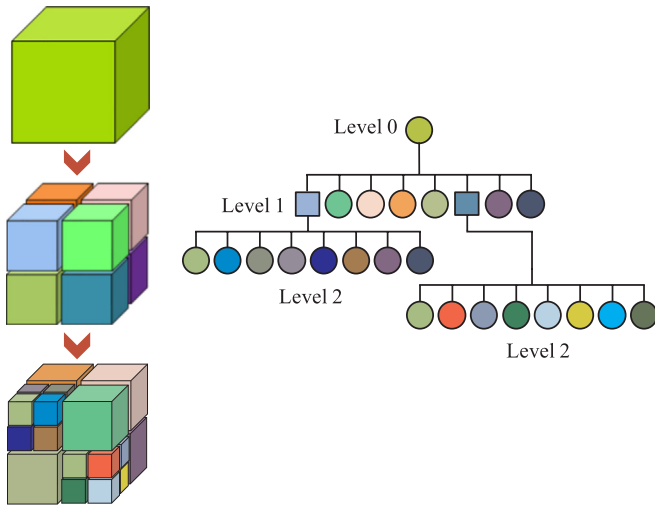


Fig. 3-1. Octree representation.

3.2. Uniform scale grid

As can be seen in Fig. 2-1, the minimum thickness of the face slab is only 0.4 m, but the rock can extend to a length of more than 1700 m. The large size of the slab makes it very difficult to generate desirable grids. Currently, uniform scale grids are popular, and their satisfactory performance has been witnessed; when the capacity of a grid needs to be enhanced while dealing with structures that are sensitive to variations in stress, a common uniform scale mesh can be used, as seen in Fig. 3-3(a). This density of mesh is sufficient for capturing the stress and displacement variations of rock and rockfill; however, this density is far from adequate for the analysis of a concrete face slab. An optional solution is given in Fig. 3-3(b), namely, a refinement grid is recommended.

A uniform mesh means that the element size is roughly identical along one direction or in all directions. Thus, the number of elements will dramatically increase with decreasing size; moreover, massive

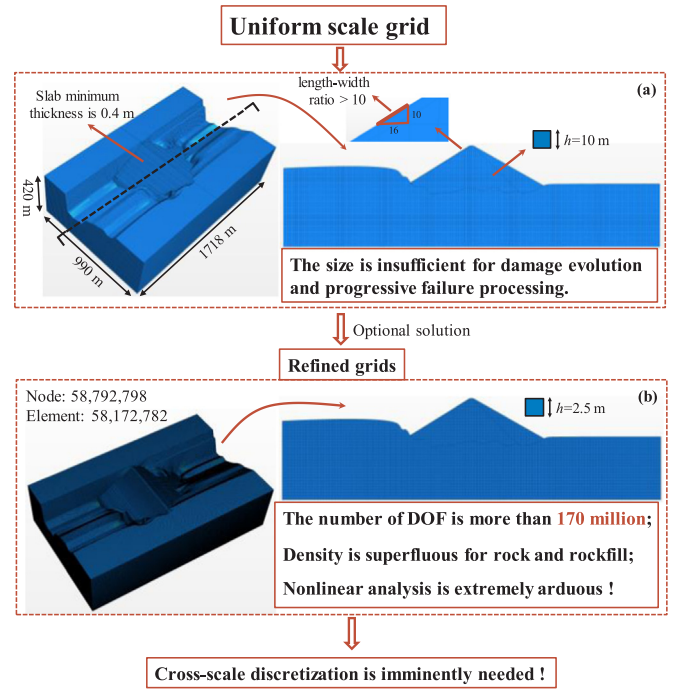


Fig. 3-3. Uniform scale mesh generation.

grids are superfluous for improving computational precision. Using the aforementioned model as an example, 58,172,782 elements will be produced when the size of the face slab is refined to approach 3.0 m, resulting in more than 170 million degrees of freedom. Obviously, such a scale model is extremely arduous, even infeasible, for elasto-plastic analysis. Furthermore, the number of elements of important structures occupies less than 10%, meaning that massive computing resources will be wasted. Therefore, a breakthrough technique should be explored to avoid this phenomenon.

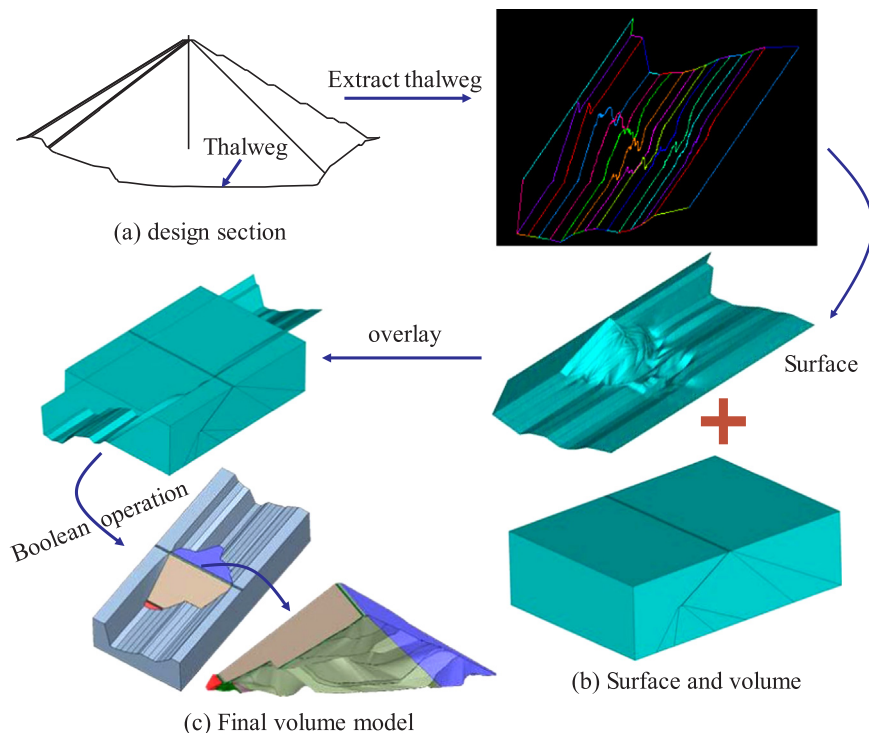


Fig. 3-2. The process of generating a volume model.

3.3. Cross-scale mesh discretization

To circumvent the intractable problems associated with elaborate three-dimensional modelling, the use of the cross-scale grid scheme is highly recommended. There are a few optional technologies, including the substructure technique, the multipoint restriction method master-slave structure method and the discrete element coupled finite element method. Although these methods have been used to solve many simulation problems, they actually have a secondary analysis framework, meaning that these models are actually solved via two steps. For example, in DEM-FEM analyses, first, a part of the structure is analyzed using DEM; second, these displacement and stress solutions are considered as boundary conditions that are loaded on the remainder part and then calculated using FEM. The process then undergoes an alternately recursive computation until the accuracy of the solution is satisfied. This secondary iteration analysis pattern will generate certain errors, and even incorrect results, in elastoplastic simulations; thus, more efforts should be devoted to avoid this deficiency. Therefore, a concurrent cross-scale mesh generation method is adopted in this paper.

3.3.1. Mesh generation

When building the volume model for the high concrete-faced rockfill dam, we discretize the spatial domain in a hierarchy of grids with an octree generator. To guarantee precision and save computer resources, l_{\max} and l_{\min} are defined as the maximum and minimum layers of grids, respectively. They are defined as 20 m and 1.25 m in this model, respectively. More schematic information can be seen in Fig. 3–4, where the numbers of elements and nodes are 657,328 and 732,505, respectively, and the total number of degrees of freedom is close to 2200 thousand, while the entire time consumed in the discretization is only 182 s. This method provides an attractive alternative for efficient cross-scale analysis, which can dramatically accelerate the process of mesh generation for large-scale complex engineering structures.

Another unique feature is that a hybrid octree-based mesh, instead of a pure octree, is adopted in this study. Compared to the pure octree technique, the former technique is more accurate in approximating boundaries using fewer elements and reducing the number of DOFs, thus resulting in the greater efficiency of the computation and making it preferable for grid generation. A schematic illustration of this mesh is exhibited in Fig. 3–5.

It is obvious that this method removes the bottleneck in the rapid automation of mesh generation for complex geometries, while the grids satisfy all of the restrictions mentioned in Section 2. The reasons for this improvement are discussed as follows.

To model the impervious slab, which plays the most crucial role in dam safety, a dense mesh is adopted with a maximal size of less than 2 m, where the variations in stresses can be captured. This can be seen in Fig. 3–6. The structure is divided by horizontal and vertical lines, thus inherently satisfying the demands of interface joints. The same principle appears in the dam body, allowing the horizontal stratification to be possessed automatically. Another significant advantage is the thalweg can be described meticulously, thus providing a more practical model for calculations.

The last feature is the cross-scale strategy, where coarse grids are sufficient for the simulation of elastic rock, a relatively coarse mesh is employed for the dam body due to the lower stress gradient, and a dense gridding is used in the interface between the two materials and vital structures, such as the slab and high toe wall, in order to obtain more reasonable results. Additionally, a considerable number of elements can be economized using this scheme, thus resulting in improved simulation efficiency.

3.3.2. Mesh feature

The problems associated with the modelling of high CFRDs can seemingly be solved by using an octree-based mesh. However, a new difficulty is introduced when using the established model, which is shown in Fig. 3–7. There are numerous traditional element shapes, such

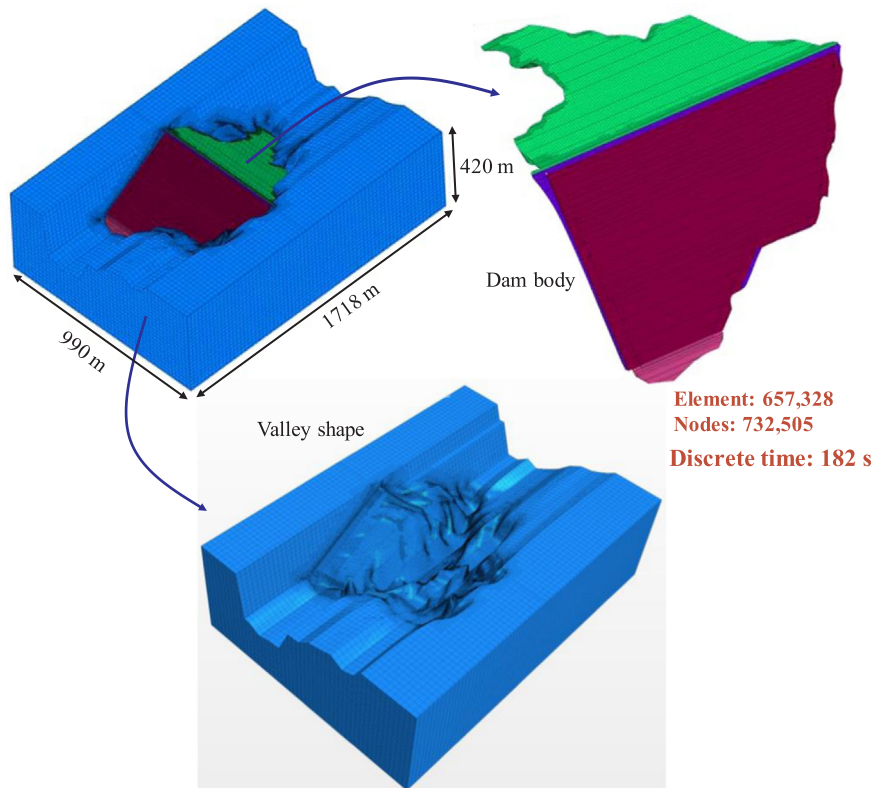


Fig. 3–4. Octree-based mesh of a high concrete-faced rockfill dam.

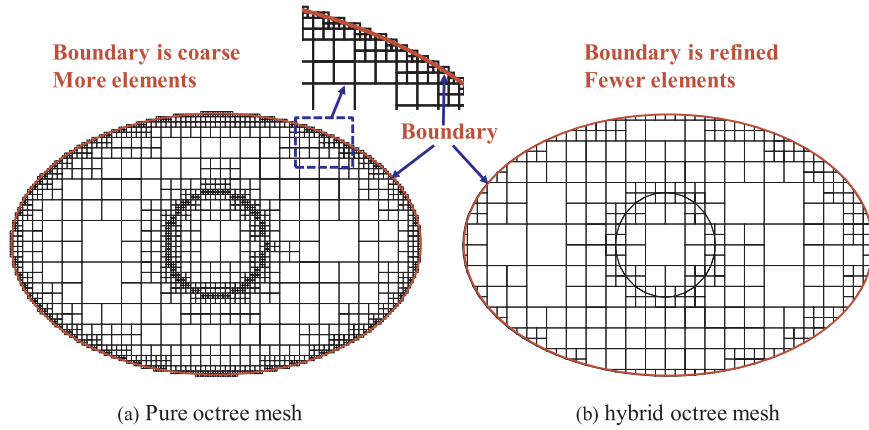


Fig. 3–5. Features of different octree-based meshes.

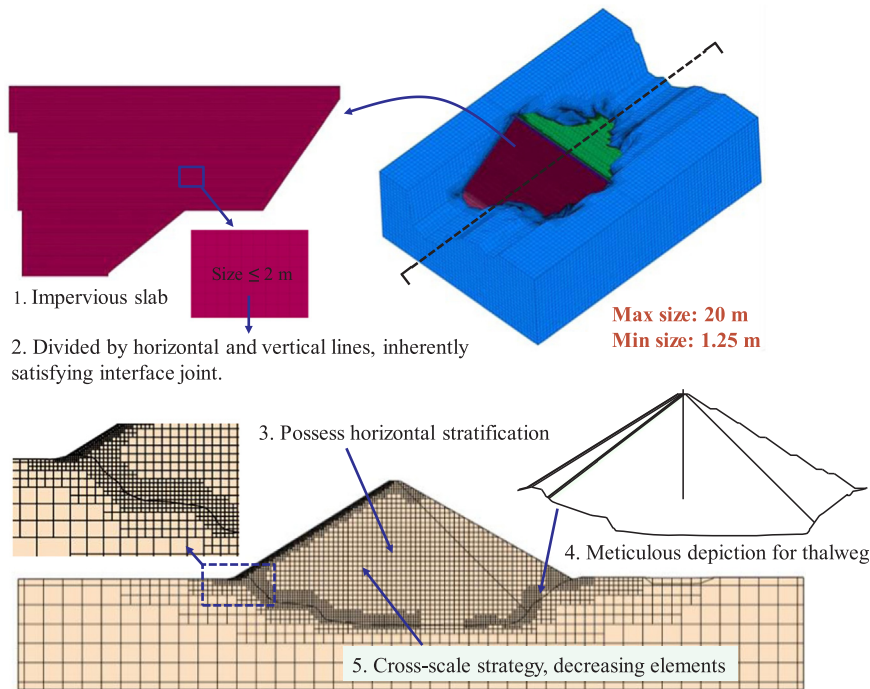


Fig. 3–6. Detailed display of octree-based mesh.

as tetrahedrons, pentahedrons and hexahedrons, which can be directly solved using the conventional finite element analysis method. However, a small number of complex elements (polyhedrons) exist in the model, which fall beyond the capabilities of conventional formulations.

In this situation, a multipurpose element technique must urgently be explored; in doing so, its many applications can be assessed.

4. Element solving technique

For the sake of jumping out the embarrassed situation, a polyhedron finite element method can be introduced. Here, we recommend using the scaled boundary finite element method (SBFEM) due to its extraordinary capabilities.

4.1. Scaled boundary Polyhedron finite element method

SBPFE is chosen because of its convenience. This method combines the advantages of the finite element method (FEM) and boundary element method (BEM) [18,19], and it also contains the flexibility

inherited from polyhedrons. This method is also semi-analytical and can decrease the spatial computation by one dimension, resulting in only a plane interpolation function being needed for 3D problems; this function is straightforward to modify and derive formulations for computing polyhedron elements, making it different than many other numerical methods.

In order to establish a comprehensive element technique, the mean-value polygon (in which the number of element sides is no less than 3) interpolation method is introduced because of its desirable properties [44,45] and straightforward ability to be programmed. The decomposition diagram of a complex element containing pentagonal boundary surfaces is shown in Fig. 4-1. Other boundary shapes, such as triangles, quadrangles, hexagons and arbitrary polygons, are also solvable, as has been described in the literature [43,45]. These formulas are listed in Eqs. (4)–(1) and (4)–(2).

$$\psi_i(\mathbf{x}) = \frac{w_i(\mathbf{x})}{\sum_{j=1}^n w_j(\mathbf{x})} \quad (4-1)$$

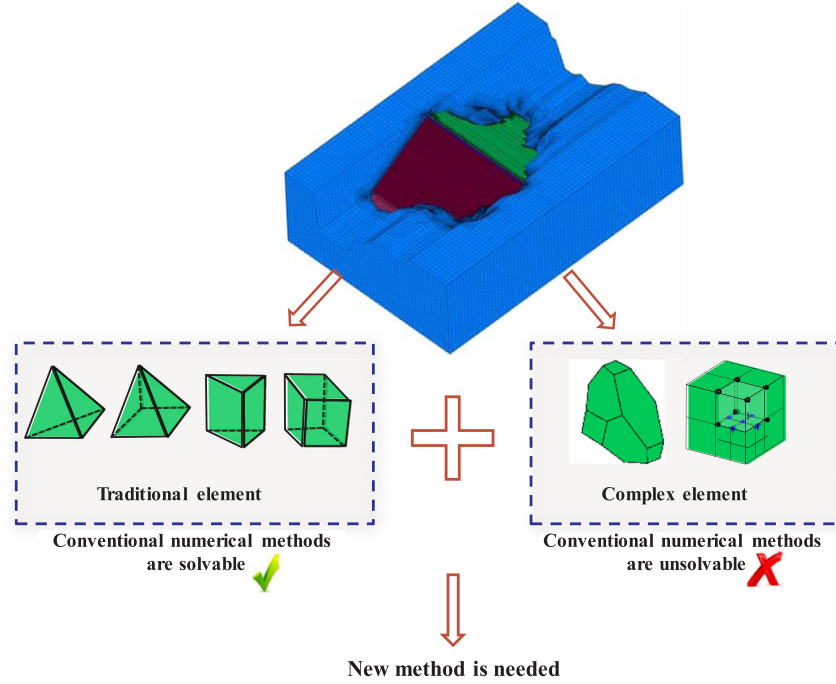


Fig. 3–7. Detailed display of octree-based mesh.

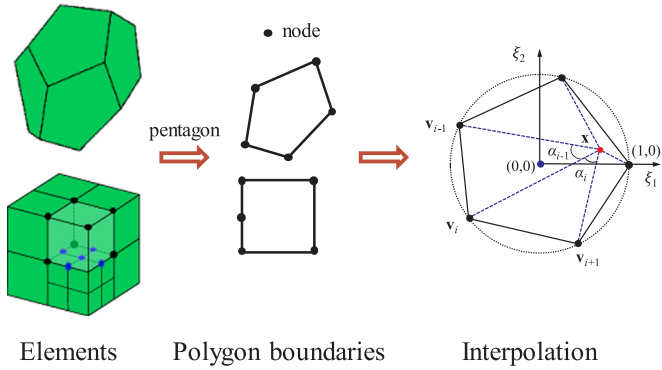


Fig. 4–1. Interpolation for the polygon boundaries of complex elements.

$$w_i(\mathbf{x}) = \frac{\tan(\alpha_{i-1}/2) + \tan(\alpha_i/2)}{\|\mathbf{x} - \mathbf{v}_i\|} \quad (4-2)$$

Where $\psi_i(\mathbf{x})$ is the interpolating function, $w_i(\mathbf{x})$ is the mean-value weight function, and $\|\mathbf{x} - \mathbf{v}_i\|$ is the Euclidean distance between \mathbf{x} and \mathbf{v}_i .

As it can be seen in Fig. 4–2, an arbitrary point $P(x, y, z)$ located in the boundary can be readily interpolated using mean-value functions, which are described in Eq. (4–3).

$$\begin{aligned} x(\xi_1, \xi_2) &= \psi(\xi_1, \xi_2)x \\ y(\xi_1, \xi_2) &= \psi(\xi_1, \xi_2)y \\ z(\xi_1, \xi_2) &= \psi(\xi_1, \xi_2)z \end{aligned} \quad (4-3)$$

where \mathbf{x} , \mathbf{y} , and \mathbf{z} are the coordinate vectors of the boundary nodes. After the entire spatial plane is captured, the pyramid can be described by scaling the boundary with a dimensionless radial coordinate ξ and connecting the scaling centre O and the boundary nodes. The radial coordinate ξ varies from 0 at the scaling centre to 1 at the boundary. Therefore, the scaled outer image of the boundary is obtained by scaling the Cartesian coordinates of the boundary with the same scaling factor ξ , which can be expressed as

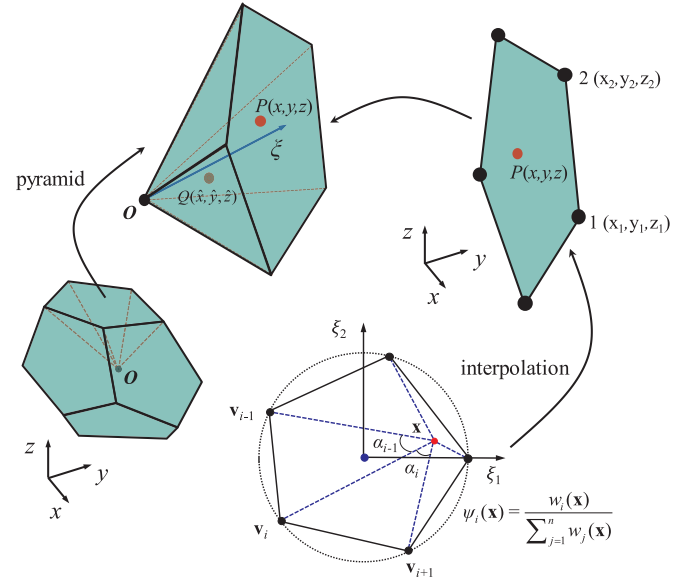


Fig. 4–2. Shape derivation decomposition for polyhedron SBFEM.

$$\begin{aligned} \hat{x}(\xi, \xi_1, \xi_2) &= \xi\psi(\xi_1, \xi_2)x \\ \hat{y}(\xi, \xi_1, \xi_2) &= \xi\psi(\xi_1, \xi_2)y \\ \hat{z}(\xi, \xi_1, \xi_2) &= \xi\psi(\xi_1, \xi_2)z \end{aligned} \quad (4-4)$$

The isoparametric mapping technique is then introduced, wherein a transformational matrix is necessary, as expressed in Eq. (4–5)

$$\mathbf{J}_m \begin{pmatrix} \xi_1, \xi_2 \end{pmatrix} = \begin{bmatrix} x(\xi_1, \xi_2) & y(\xi_1, \xi_2) & z(\xi_1, \xi_2) \\ x(\xi_1, \xi_2)_{,\xi_1} & y(\xi_1, \xi_2)_{,\xi_1} & z(\xi_1, \xi_2)_{,\xi_1} \\ x(\xi_1, \xi_2)_{,\xi_2} & y(\xi_1, \xi_2)_{,\xi_2} & z(\xi_1, \xi_2)_{,\xi_2} \end{bmatrix} \quad (4-5a)$$

$$|\mathbf{J}_m(\xi_1, \xi_2)| = x(y_{\xi_1, \xi_2} z_{,\xi_2} - z_{,\xi_1} y_{\xi_2}) + y(z_{,\xi_1} x_{,\xi_2} - x_{,\xi_1} z_{,\xi_2}) + z(x_{,\xi_1} y_{\xi_2} - y_{\xi_1} x_{,\xi_2}) \quad (4-5b)$$

When solving a 3D problem, the displacement components of an

arbitrary point (ξ, ξ_1, ξ_2) inside a pyramid are interpolated using a presumptive radial displacement function $\mathbf{u}(\xi)$ and a mean-value shape function, which is written as Eq. (4–6), where $[\mathbf{I}]$ is the 3×3 identity matrix, and ψ_i ($i = 1, 2, 3, \dots, n$) is the nodal interpolated function defined in a canonical isoparametric element [45].

$$\mathbf{u}(\xi, \xi_1, \xi_2) = \psi^u(\xi_1, \xi_2) \mathbf{u}(\xi) \quad (4-6a)$$

$$\psi^u(\xi_1, \xi_2) = [\psi_1[\mathbf{I}], \psi_2[\mathbf{I}], \psi_3[\mathbf{I}], \psi_4[\mathbf{I}], \dots] \quad (4-6b)$$

The assumed radial function $\mathbf{u}(\xi)$, is a solution of the equilibrium Eq. (4–7), which is extracted using the mechanical equilibrium condition under the theoretical framework of the SBFEM.

$$E_0 \xi^2 \mathbf{u}(\xi)_{,\xi\xi} + (2E_0 + E_1^T - E_1) \xi \mathbf{u}(\xi)_{,\xi} + (E_1^T - E_2) \mathbf{u}(\xi) + \mathbf{F}(\xi) = 0 \quad (4-7)$$

where the coefficient matrices E_0 , E_1 , and E_2 are intermediate variables that depend only on the geometry and material properties. These coefficient matrices can be calculated using Eq. (4–8).

$$E_0 = \int_{-1}^{+1} \int_{-1}^{+1} \mathbf{B}_1^T \mathbf{D} \mathbf{B}_1 |\mathbf{J}_m| d\xi_1 d\xi_2 \quad (4-8a)$$

$$E_1 = \int_{-1}^{+1} \int_{-1}^{+1} \mathbf{B}_2^T \mathbf{D} \mathbf{B}_1 |\mathbf{J}_m| d\xi_1 d\xi_2 \quad (4-8b)$$

$$E_2 = \int_{-1}^{+1} \int_{-1}^{+1} \mathbf{B}_2^T \mathbf{D} \mathbf{B}_2 |\mathbf{J}_m| d\xi_1 d\xi_2 \quad (4-8c)$$

where \mathbf{B}_1 and \mathbf{B}_2 are transition matrices, \mathbf{D} is the material constitutive matrix, and ψ is the polygonal shape function for a boundary surface.

The equilibrium equation is solved via the mathematical theorem and eigenvalue decomposition technique. Ultimately, the solution is given as Eq. (4–9)

$$\mathbf{u}(\xi) = \varphi_u \xi^{-(0.5I+S_n)} \mathbf{c} \quad (4-9)$$

where S_n is a diagonal matrix, \mathbf{I} is an identity matrix, and the entries comprise the real parts of the eigenvalues. The matrix φ_u comprises the modal displacements, and its size depends on the degrees of freedom (DOF) of the surface elements. The coefficient \mathbf{c} is the integration constant, which can be calculated from the boundary nodal displacement vector $\mathbf{u}_b = \mathbf{u}(\xi = 1)$.

$$\mathbf{c} = \varphi_u^{-1} \mathbf{u}_b \quad (4-10)$$

The final formula of the radial displacement $\mathbf{u}(\xi)$ can be stated as

$$\mathbf{u}(\xi) = \varphi_u \xi^{-S_n-0.5I} \varphi_u^{-1} \mathbf{u}_b \quad (4-11)$$

The displacement field $\mathbf{u}(\xi, \xi_1, \xi_2)$ of the polyhedral element can be evaluated by substituting Eq. (4–11) into Eq. (4–6a).

$$\mathbf{u}(\xi, \xi_1, \xi_2) = (\psi^u(\xi_1, \xi_2) \varphi_u \xi^{-(0.5I+S_n)} \varphi_u^{-1}) \mathbf{u}_b \quad (4-12)$$

Therefore, the polyhedral element shape function $\Phi(\xi, \xi_1, \xi_2)$, which is formulated based on SBFEM, is shown in Eq. (4–13).

$$\Phi(\xi, \xi_1, \xi_2) = \psi^u(\xi_1, \xi_2) \varphi_u \xi^{-(0.5I+S_n)} \varphi_u^{-1} \quad (4-13)$$

Using the strain field formulation provided by Wolf and Song [17], the strain field of a polyhedron can be rewritten by substituting in Eq. (4–11) as follows:

$$\begin{aligned} \varepsilon(\xi, \xi_1, \xi_2) &= (\mathbf{B}_1(\xi_1, \xi_2) \varphi_u (-S_n - 0.5) \xi^{-(1.5I+S_n)} \varphi_u^{-1}) \mathbf{u}_b \\ &\quad + \left(\frac{1}{\xi} \mathbf{B}_2 \left(\xi_1, \xi_2 \right) \varphi_u \xi^{-(0.5I+S_n)} \varphi_u^{-1} \right) \mathbf{u}_b \end{aligned} \quad (4-14)$$

By extracting the coefficient before \mathbf{u}_b , the strain fields of the scaled boundary finite element can be simplified as

$$\varepsilon(\xi, \xi_1, \xi_2) = \mathbf{B}(\xi, \xi_1, \xi_2) \mathbf{u}_b \quad (4-15a)$$

$$\begin{aligned} \mathbf{B}(\xi, \xi_1, \xi_2) &= (\mathbf{B}_1(\xi_1, \xi_2) \varphi_u (-S_n - 0.5) \xi^{-(1.5I+S_n)} \varphi_u^{-1}) \\ &\quad + \left(\frac{1}{\xi} \mathbf{B}_2 \left(\xi_1, \xi_2 \right) \varphi_u \xi^{-(0.5I+S_n)} \varphi_u^{-1} \right) \end{aligned} \quad (4-15b)$$

where $\mathbf{B}(\xi, \xi_1, \xi_2)$ is the strain-displacement matrix of the polyhedral element.

Using the principle of virtual work, the scaled boundary polyhedron formulation for elasto-plastic is performed, which can be expressed as Eq. (4–16).

$$\begin{aligned} \left(\int_{\Omega} \mathbf{B}^T(\xi, \xi_1, \xi_2) \mathbf{D}_{ep} \mathbf{B}(\xi, \xi_1, \xi_2) d\Omega \right) \Delta \mathbf{u}_b &= \left(\int_{\Gamma} \Phi^T(\xi, \xi_1, \xi_2) \mathbf{f}_i d\Gamma + \int_{\Gamma} \Phi^T(\xi, \xi_1, \xi_2) \mathbf{f}_b d\Omega \right) \\ &\quad - \left(\int_{\Omega} \mathbf{B}^T(\xi, \xi_1, \xi_2) \sigma(\xi, \xi_1, \xi_2) d\Omega \right) \end{aligned} \quad (4-16)$$

Then, three steps must be conducted. First, a polyhedral formulation of the elasto-plastic stiffness matrix must be obtained, as shown in Eq. (4–16).

$$\mathbf{K}_{ep} = \int_{\Omega} \mathbf{B}^T(\xi, \xi_1, \xi_2) \mathbf{D}_{ep} \mathbf{B}(\xi, \xi_1, \xi_2) d\Omega \quad (4-17)$$

The \mathbf{K}_{ep} value of the polyhedron is determined by integrating over each pyramid with quadrature points [24].

$$\mathbf{K}_{ep} = \sum_{i=1}^{m \cdot p_k} \mathbf{B}^i(\xi, \xi_1, \xi_2) \mathbf{D}_{ep}^i \mathbf{B}^i(\xi, \xi_1, \xi_2) V_i \quad (4-18)$$

where m represents the number of surfaces in the polyhedron, p_k denotes the total number of quadrature points in the k^{th} surface, $\mathbf{B}^i(\xi, \xi_1, \xi_2)$ represents the strain displacement transformation matrix computed on the i^{th} Gauss point, \mathbf{D}_{ep}^i expresses the elasto-plastic constitutive matrix of the i^{th} Gaussian point and is calculated from the given plasticity model, and V_i is the volume occupied by the i^{th} point in V_e . The global elasto-plastic stiffness matrix of the solved domain can be evaluated after the \mathbf{K}_{ep} values of all of the polyhedrons have been computed.

Secondly, the external load vector \mathbf{R}_{ext} can be extracted from Eq. (4–16); it is expressed as

$$\mathbf{R}_{ext} = \int_{\Gamma} \Phi^T(\xi, \xi_1, \xi_2) \mathbf{f}_i d\Gamma + \int_{\Omega} \Phi^T(\xi, \xi_1, \xi_2) \mathbf{f}_b d\Omega \quad (4-19)$$

The first term on the right-hand side of Eq. (4–19) is the distributed load on the boundary. It can be further simplified by considering that $(\xi = 1) \Phi(\xi, \xi_1, \xi_2) = \lambda^u(\xi_1, \xi_2)$ applies at the boundary; this can be rewritten as

$$\int_{\Gamma} \Phi^T(\xi, \xi_1, \xi_2) \mathbf{f}_i d\Gamma = \int_{-1}^1 \lambda^u(\xi_1, \xi_2) |\mathbf{J}(\xi_1, \xi_2)| \mathbf{f}_i d\xi_1 d\xi_2 \quad (4-20)$$

The second term is the body load vector. For the case of a constant body load, this term is expressed using numerical integration with the Gaussian points

$$\int_{\Omega} \Phi^T(\xi, \xi_1, \xi_2) \mathbf{f}_b d\Omega = \sum_{k=1}^m \sum_{i=1}^{p_k} [\lambda_{ki}^u(\xi_1, \xi_2) \varphi_u \xi_i^{-(0.5I+S_n)} \varphi_u^{-1}]^T \mathbf{f}_b V_{ki} \quad (4-21)$$

The formulation of the load vector that results from the internal stresses is defined in Eq. (4–22), which is obtained from Eq. (4–16).

$$\mathbf{R}_{int} = \int_{\Omega} \mathbf{B}^T(\xi, \xi_1, \xi_2) \sigma(\xi, \xi_1, \xi_2) d\Omega \quad (4-22)$$

Here, the Gaussian numerical integration is introduced into the summation. First, the strain field $\varepsilon(\xi, \xi_1, \xi_2)$ can be calculated using Eq. (4–15a) after the nodal displacements \mathbf{u}_b on the boundary are determined. Next, the stress field $\sigma_i(\xi, \xi_1, \xi_2)$ on each Gauss point is captured by substituting the elasto-plastic constitutive matrix \mathbf{D}_{ep}^i and this formulation is expressed as

$$\mathbf{R}_{int} = \sum_{k=1}^m \sum_{i=1}^{p_k} \mathbf{B}^{ki}(\xi, \xi_1, \xi_2)^T \sigma_{ki}(\xi, \xi_1, \xi_2) V_{ki} \quad (4-23)$$

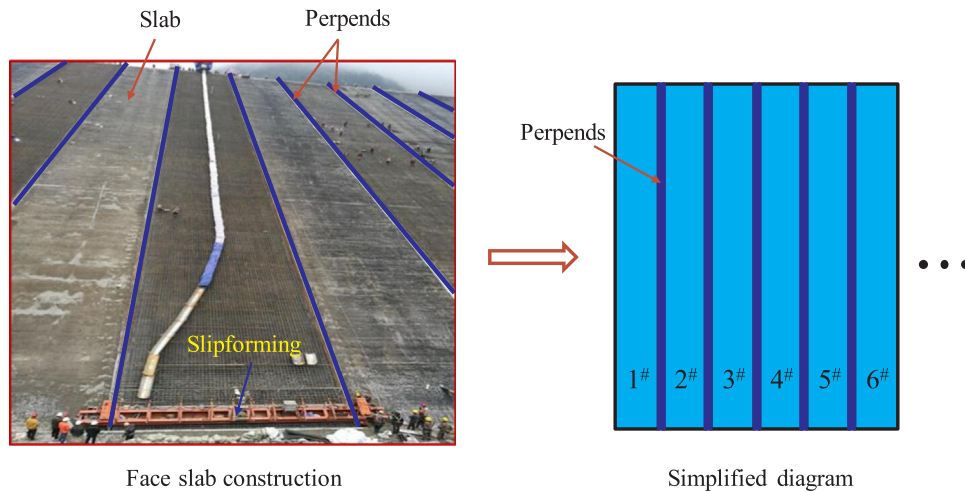


Fig. 4-3. Spatial locations of perpendents (vertical joints).

4.2. Cross-scale interface element

A zone with different mechanical characteristics exists between soils (rockfill) and the concrete face slab due to the large differences in their mechanical properties. Interface elements are versatile tools that are widely used in modelling the relative displacements of the zones between soils and structures. Many investigations have been conducted [46–50], which indicated that the behaviours of soil-structure interfaces can be crucial to the overall response of a soil-structure system; therefore, the simulation of an interface zone is necessary in the modelling of a CFRD system. These elements are located between the rockfill and face slab as well as between the rock and slab, wherein different material properties can be observed. Additionally, perpendents are set between the face slab itself because their width is specified and they facilitate construction. In the graph shown in Fig. 4-3, the width of the slab is determined to range from 7.5 m to 15 m, and an overall view of the system is displayed in Fig. 4-4.

As a cross-scale octree-based grid is first utilized in the calculation of a CFRD, interfaces are installed between the soils and face slab, rock and face slab, and toe slab and face slab, as well as in the slab itself; these perpendents are also cross-scaled, and one of the surfaces inevitably

contains multiple shapes, including triangles, quadrangles and arbitrary polygons. Conventional interface elements are composed of triangles and quadrangles due to the extrusion of the surfaces of traditional elements (shown in Fig. 3-6), making it impossible to directly apply this technique to cross-scale interfaces. An enhanced element that can simultaneously manage the triangle, quadrangle and polygon interface elements should be explored to circumvent this deficiency.

4.2.1. Theoretical generalization

Generally, an interface element consists of two uniform surfaces (top and bottom, see Fig. 4-5), and the number sorting of nodes follows the right-hand rule. The novel element evidently possesses fascinating flexibility, which is more versatile and removes the restriction of shape types from this method.

We assume that the nodal displacement vector δ is equal to $\{u \ v \ w\}$, where u , v and w represent the displacements along the x -, y - and z -directions, respectively. The vector δ , which is associated with the top and bottom surfaces, can be calculated based on the 2D mean-value polygon element shape function.

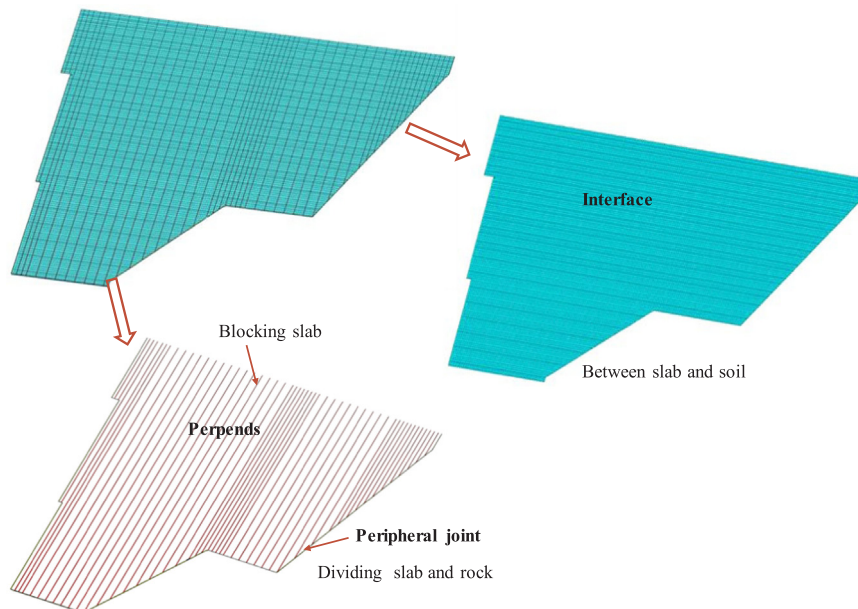


Fig. 4-4. Spatial interface, perpendents and peripheral joint elements.

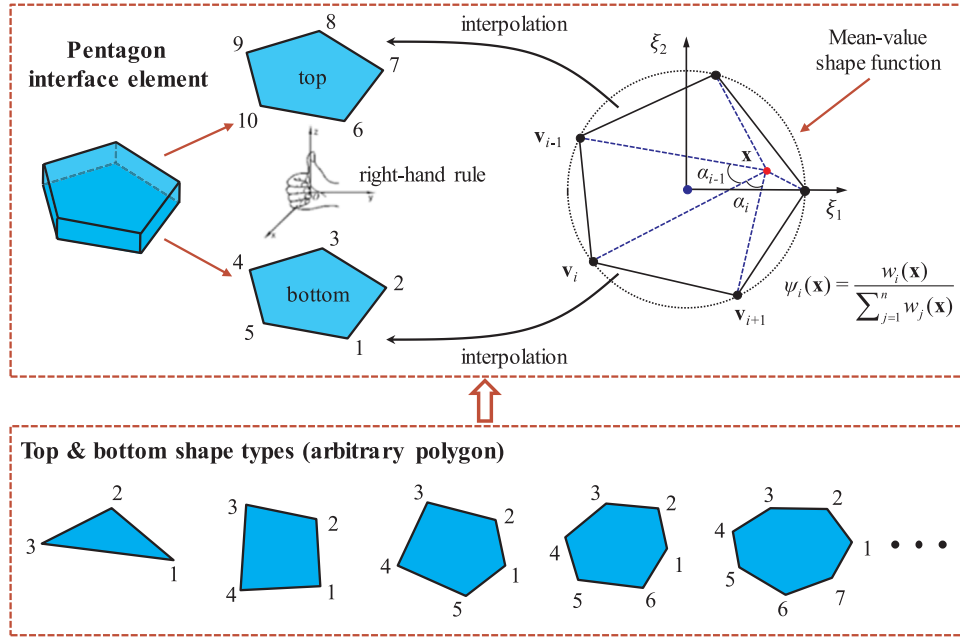


Fig. 4-5. Explanation of arbitrary polygon interface elements.

$$\delta = [\psi_1 \ \psi_2 \ \psi_3 \ \psi_4 \ \dots] \begin{Bmatrix} \delta_1 \\ \delta_2 \\ \delta_3 \\ \delta_4 \\ \vdots \end{Bmatrix} \quad (4-24)$$

The relative displacement $\{d\}$ between the top and bottom surfaces is determined as follows:

$$d = \delta^{top} - \delta^{bottom} = B^e \delta^e \quad (4-25)$$

where

$$B^e = \begin{bmatrix} \psi_1^{top} I & \psi_2^{top} I & \psi_3^{top} I & \psi_4^{top} I & \dots & -\psi_1^{bottom} I & -\psi_2^{bottom} I & -\psi_3^{bottom} I & -\psi_4^{bottom} I & \dots \end{bmatrix} \quad (4-26)$$

$$\delta^e = [\delta_1^{top} \ \delta_2^{top} \ \delta_3^{top} \ \delta_4^{top} \ \dots \ \delta_1^{bottom} \ \delta_2^{bottom} \ \delta_3^{bottom} \ \delta_4^{bottom} \ \dots]^T \quad (4-27)$$

I is a 3×3 identity matrix.

The stiffness matrix K is determined using Eq. (4-28), where D is the constitutive matrix and J is the Jacobian matrix.

$$K = \int_0^1 \int_0^1 B^e D B^e |J| d\xi_1 d\xi_2 \quad (4-28)$$

4.2.2. Single element

Fig. 4-6 presents a typical proposed interface element that is used as a verification example. First, a linear elastic material is simulated, and the parameters are defined as: $k_n = 1.0 \times 10^9$ Pa/m and $k_s = 1.0 \times 10^6$ Pa/m. The element is subjected to a surface compressive load of $p = 100$ kPa. Simultaneously, a surface shear traction of $T_x = 10$ kPa is applied at the top surface. As summarized in Table 4-1, the displacement of the nodes at the top surface are equivalent to the exact solution, which is given as follows:

$$\delta_y = p/k_n = -1.0 \times 10^{-4} \text{ m and } \delta_x = T_x/k_s = 1.0 \times 10^{-4} \text{ m} \quad (4-29)$$

In the case of elasto-plastic material, the cyclic loading direct shear test of the interface conducted in the literature [51,52] is used to verify the validity of the proposed interface element. The normal surface stress p is 2.0 MPa, and the cyclic shear displacement T_x ($0 \rightarrow 35 \rightarrow -35 \rightarrow 15$ mm) is loaded slowly via 2215 steps. A generalized plastic

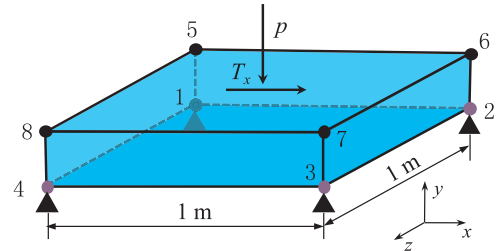


Fig. 4-6. Interface test for linear elastic and elasto-plastic behavior.

Table 4-1

Results of the interface test performed with linear elastic material.

node	$\delta_x / 10^{-4} \text{ m}$	$\delta_y / 10^{-4} \text{ m}$
5	1.0000000	-1.0000000
6	1.0000000	-1.0000000
7	1.0000000	-1.0000000
8	1.0000000	-1.0000000

interface model [49,51] is utilized to capture the properties of the interface, and the parameters [52] are given in Table 4-2. As illustrated in Fig. 4-7, the result is in good agreement compared with that obtained in reference [52], which indicates that the accuracy of the proposed polygon interface element is satisfactory.

4.2.3. Sliding block

As is shown in Fig. 4-8, a sliding block is placed on a foundation. The linear model is adopted, where the density is 1250 kg/m^3 , the elasticity modulus is $E = 2.4 \times 10^{10} \text{ Pa}$, and the Poisson's ratio is

Table 4-2

Parameters of the generalized plastic interface model.

Elastic modulus		Critical state			Particle breakage		
D_{s0}/kPa	D_{n0}/kPa	M_c	$e_{\tau 0}$	λ	$a/\text{kPa}^{0.5}$	b	c
1000	1500	0.88	0.4	0.091	224	0.06	3.0
Plastic direction		Plastic modulus		Loading direction			
α	r_d	k	H_0/kPa	f_h	k_m	M_f	
0.65	0.2	0.5	8500	2	0.6	0.65	

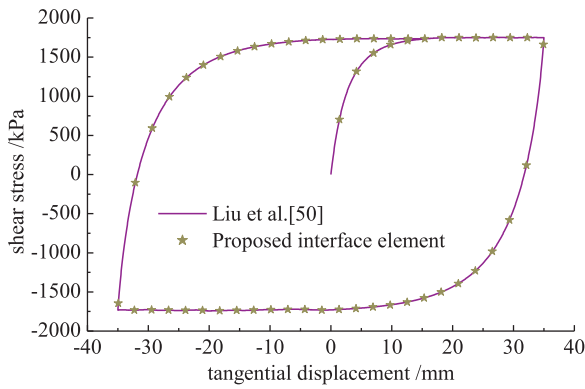


Fig. 4-7. Relationship between the shear displacement and shear stress of the interface.

$\nu = 0.163$. A uniform pressure of $P = 20 \text{ kN}$ is applied on top of the sliding block, and a uniform thrust of $F = 1.04 \times 10^7 \text{ N}$ is loaded on the bottom. The developed polygon interface element is introduced to simulate the interaction between the foundation and block, and an ideal elasto-plastic contact surface model is employed. The parameters are defined as $K_{s0} = 1.2 \times 10^8 \text{ Pa/m}$ and $K_{n0} = 2.4 \times 10^8 \text{ Pa/m}$, and the shear strength of the interface is assumed to be $f = 0.5$.

All loads are divided into 1000 steps, and the final results are exhibited in Fig. 4-9. Obviously, the total shear force of the polygon interface approaches the shear strength when loading to step 961, and the displacement of point A is continuously changing. This result is identical to the analytical solution obtained based on the ideal elasto-plastic theory. After this point, the components undergo a growth spurt, and the calculation loses convergence.

5. Numerical calculation

A cross-scale refined grid was established within 3 min using the octree-based technique; detailed information about this method can be seen in Figs. 3-4 and 3-6. In this section, an integrated elasto-plastic numerical investigation is conducted.

5.1. Material parameter identification

The staged construction of the dam is considered in the analysis, and the construction process is simulated by controlling the birth and death of elements. In this regard, the dam body is supposed to be built in 57 stages, and the face slab is alternately casted to the dam body. The water level is subsequently impounded to an elevation of 240 m in 48 steps. A detailed depiction of this process is provided in Fig. 5-1. The initial stresses from this procedure are also computed and subsequently

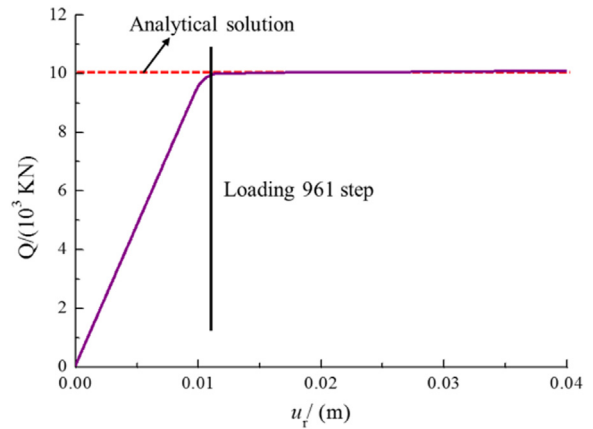


Fig. 4-9. Relationship between the displacement u_r and thrust Q of the polygon interface during loading.

applied in one increment before the seismic analysis.

A modified generalized plasticity model [5,23] of the rockfill is adopted for the static construction simulation, which was measured using large triaxial experiments. The parameters are listed in Tables 5-1 to 5-3. The concrete materials are simulated using a linear model, including the face slab, high toe wall, and toe slab, and the material is assumed to be homogeneous and isotropic, with a Young's modulus of $E = 31 \text{ GPa}$ and a Poisson's ratio of $\nu = 0.167$. The rock is also considered to be a linear material, with a Young's modulus of $E = 10 \text{ GPa}$ and a Poisson's ratio of $\nu = 0.2$.

5.2. Arbitrary polygon viscoelasticity artificial boundary

It is believed that the influence of radiation damping on an infinite foundation and that of the travelling wave effect on the dynamic response and stabilization of the rockfill dam cannot be considered using a traditional rigid boundary. Therefore, the application of a viscoelasticity artificial boundary is more reasonable for the calculation of CFRDs. Furthermore, the current boundary elements are identical to those of traditional structure grids, meaning that the polyhedrons are outside of their competence.

On the other hand, the generation of polyhedral elements using the octree technique is inevitable. To generate elements that blend automatically and seamlessly with the octree mesh, an arbitrary polygon viscoelasticity artificial boundary is explored, which exhibits automatic generation and contains a corresponding loading input algorithm. As expressed in Fig. 5-2(a), the number of polygon elements in a common boundary situation is minor. However, this number will rapidly increase when the boundary becomes more complex, as shown in Fig. 5-

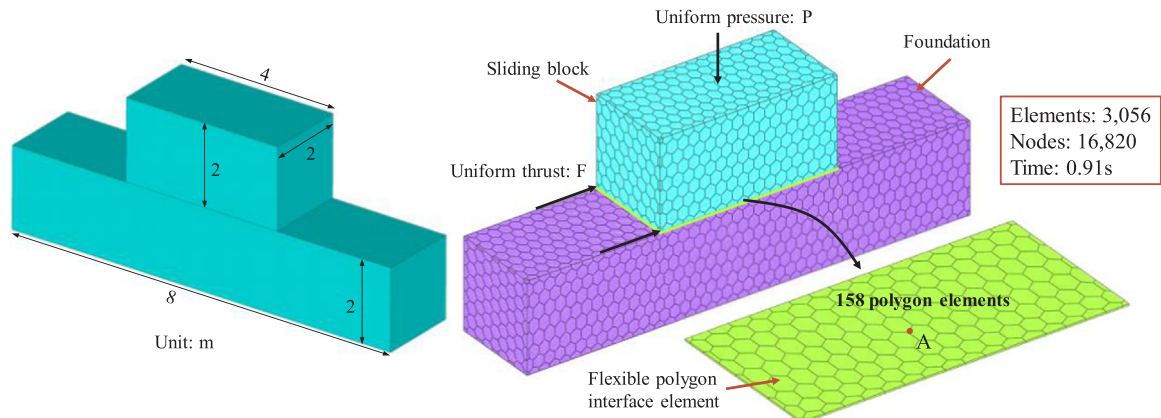


Fig. 4-8. Geometry and polyhedron mesh of sliding block.

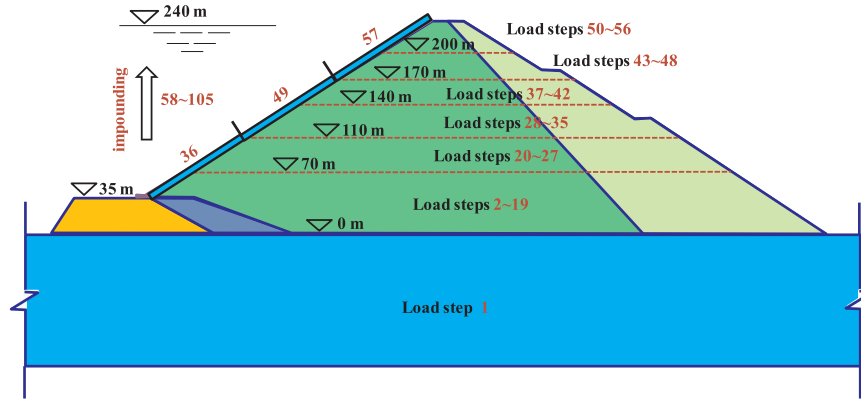


Fig. 5-1. Depiction of construction progress for the concrete-faced rockfill dam.

Table 5-1

Rockfill I material parameters in the modified generalized plasticity model.

G_0	K_0	M_g	M_f	α_f	α_g	H_0	H_{U0}	m_s
1021	1362	1.70	1.53	0.11	0.11	650	1300	0.44
m_v	m_l	m_u	r_d	γ_{DM}	γ_u	β_0	β_1	
0.44	0.5	0.5	110	20	5	30	0.025	

Table 5-2

Rockfill II material parameters in the modified generalized plasticity model.

G_0	K_0	M_g	M_f	α_f	α_g	H_0	H_{U0}	m_s
880	1173	1.70	1.50	0.10	0.30	950	1900	0.24
m_v	m_l	m_u	r_d	γ_{DM}	γ_u	β_0	β_1	
0.24	0.25	0.25	110	20	5	15	0.028	

Table 5-3

Cushion material parameters in the modified generalized plasticity model.

G_0	K_0	M_g	M_f	α_f	α_g	H_0	H_{U0}	m_s
965	1288	1.68	1.30	0.10	0.40	550	1100	0.23
m_v	m_l	m_u	r_d	γ_{DM}	γ_u	β_0	β_1	
0.23	0.45	0.45	110	20	5	20	0.020	

2(b), which will make it cumbersome to perform manual modifications. The presented polygon elements are a suitable and efficient tool with which to manage this issue.

5.2.1. Verification of wave scattering problem

To verify the accuracy of the presented polygon viscoelastic artificial boundary, the scattering problem of a three-dimensional semi-circular valley is assessed. The geometric sketch, octree grids and artificial boundary mesh are illustrated in Fig. 5-3. The relevant parameters are defined as follows: valley radius $r_0 = 210$ m, material shear modulus $G = 5.292 \times 10^9$ Pa, Poisson's ratio $\nu = 1/3$, and density $\rho = 2700$ kg/m³; the displacement amplitude of the incident wave is assumed to be 1 m. A dimensionless frequency $\eta = 2r_0/\lambda = \omega r_0/\pi c_s$ is defined, where λ is the wavelength, ω is the circular frequency and the c_s represents the shear wave velocity.

We consider the dimensionless frequency η to be 0.5 and 2.0 when the wave moves vertically. The displacement response of the observing location and the approximate analytical solution are plotted in Fig. 5-4 and Fig. 5-5, where the abscissa is the relative spatial position and the ordinate expresses the displacement amplitude of the surface nodes under steady-state vibration. The calculated results are very consistent with those presented in the literature [53], which demonstrates the accuracy of the proposed method and indicates that the polygonal viscoelasticity artificial boundary can absorb the energy of the scattered wave commendably. Therefore, the presented method can be further applied to the analysis of the dynamic response of high face rockfill dams.

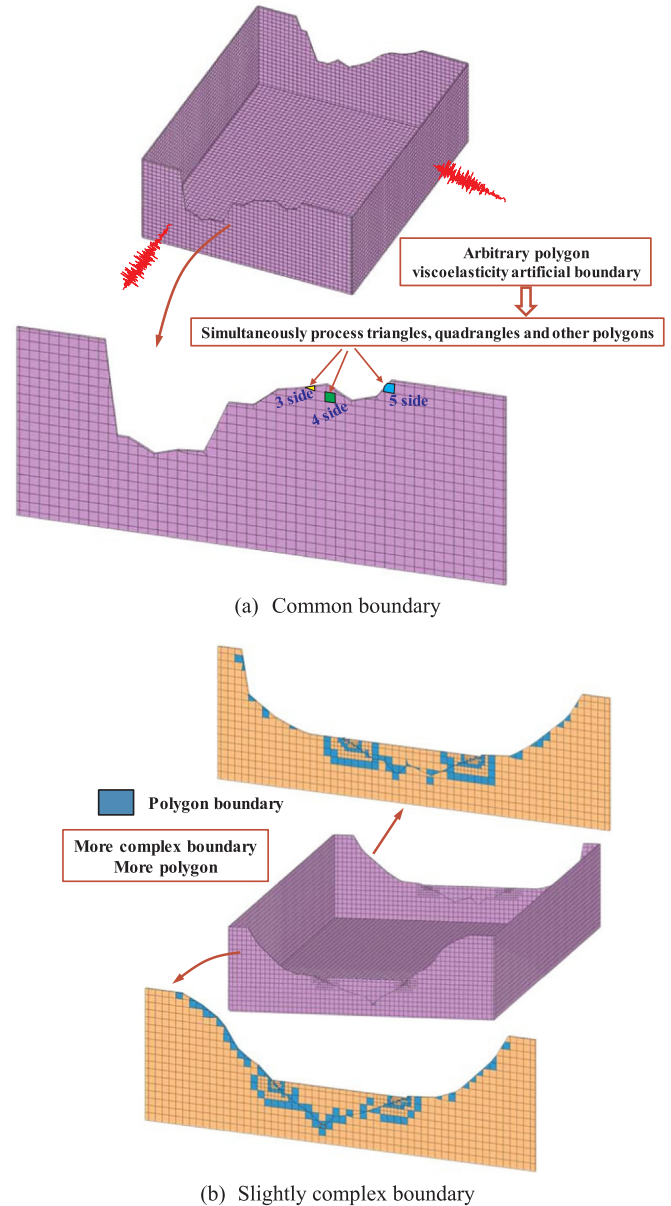


Fig. 5-2. Arbitrary polygon viscoelasticity artificial boundary elements.

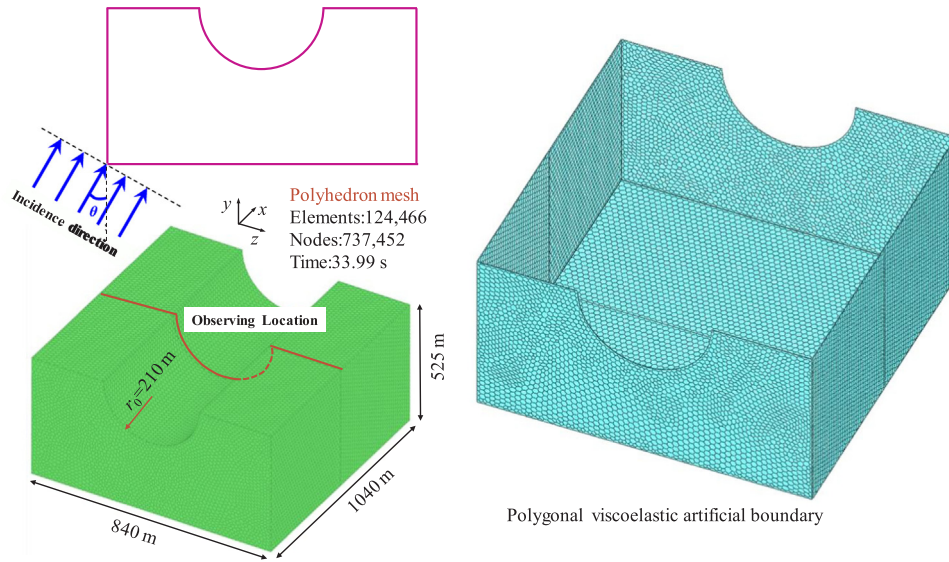


Fig. 5-3. Wave incident three-dimensional semi-circular valley (geometry, octree mesh and polygon artificial boundary).

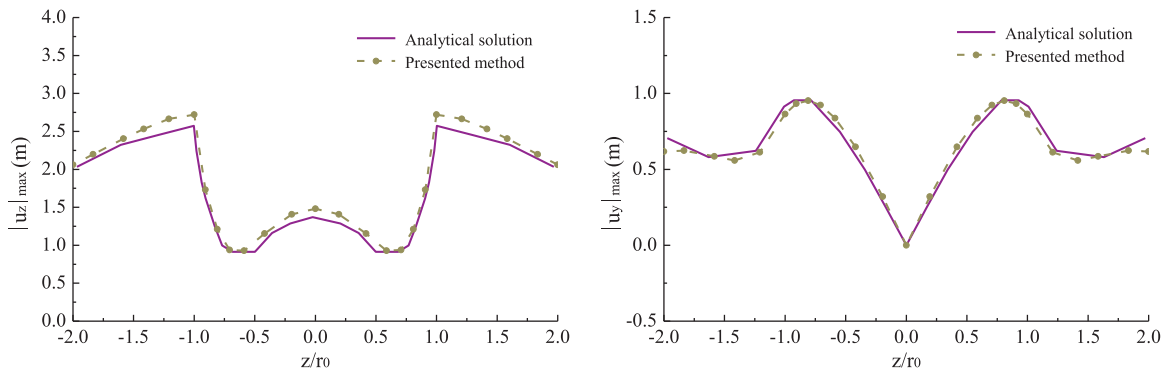


Fig. 5-4. Displacement amplitude of valley surface under the vertical incidence of $\eta = 0.5$.

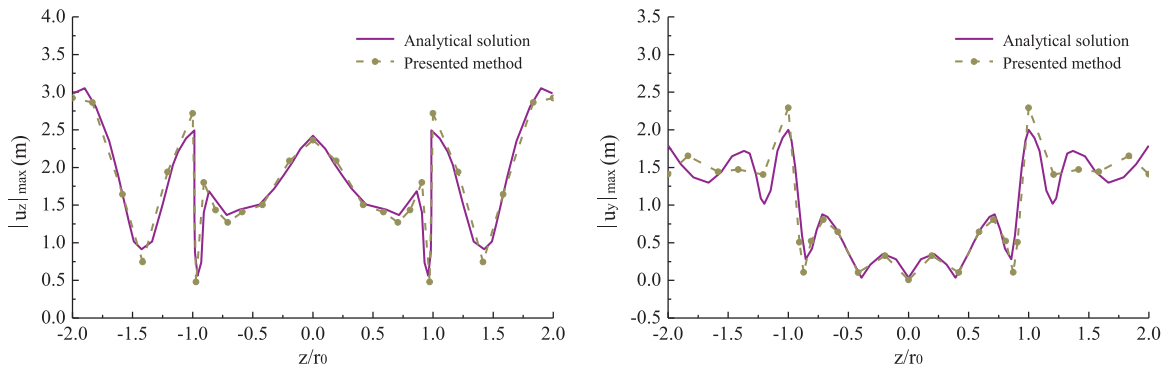


Fig. 5-5. Displacement amplitude of valley surface under the vertical incidence of $\eta = 2.0$.

5.3. Input ground motions

A modified generalized plasticity model is used for the dynamic calculation. Seismic input data with maximum accelerations measured at the foundation gallery of 0.387 g, 0.258 g and 0.387 g in the x -, y - and z -directions, respectively, are considered. The time-history records of the wave are shown in Fig. 5-6; these records are applied as the input motions with a time step of 0.01 s.

5.4. Combined computation strategy

As mentioned in Section 3.3, polytype elements are involved in the

CFRD model. These elements can be classified as two categories, namely, traditional elements and complex polyhedrons, as shown in Fig. 5-7. The specific statistics are summarized in Table 5-4; obviously, the proportion of traditional grids is 76.15%, which indicates that they comprise more than three-quarters of all grids. The remaining complex polyhedrons comprise only 23.85%, i.e., less than one-quarter of all grids.

Honestly, the scaled boundary finite element method offers more precision while requiring slightly more time than the finite element method under the condition of identical grids. Therefore, this method will partly decrease the solving efficiency when completely depending on SBPFE. However, using a combined calculation scheme, i.e., using

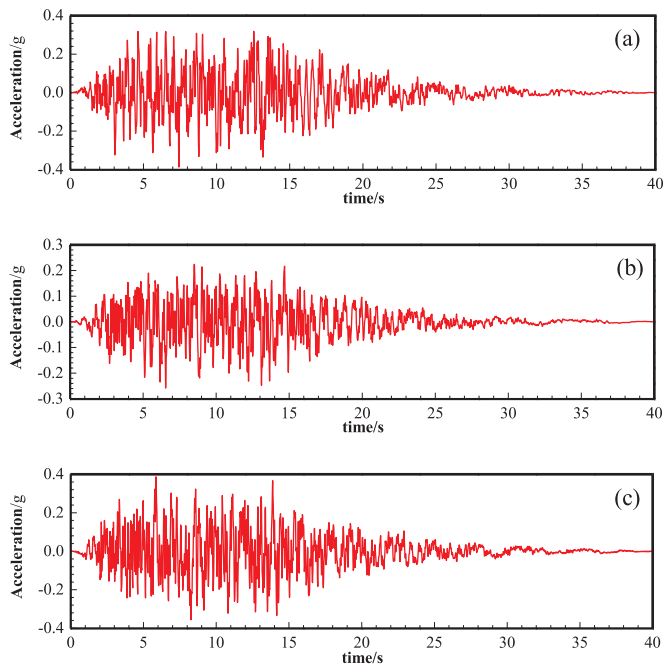


Fig. 5-6. Input acceleration records: (a) x-direction, (b) y-direction and (c) z-direction.

FEM to settle the majority of the traditional mesh and allocating SBPFE to manage the minor polyhedrons, is expected to remedy this deficiency and maximize the efficiency of each method. The use of this combination is thus strongly recommended in this paper.

5.5. Results and discussion

5.5.1. Static results

Fig. 5-8 shows the distribution of the displacement components of

Table 5-4
Statistics of the element shape types for octree-based grids.

Element shape type		Number	Percentage (%)
Traditional elements	tetrahedron	13,259	2.02
	pentahedron	81,616	12.42
	hexahedron	405,635	61.70
Polyhedrons	Faces ≥ 6	156,818	23.85

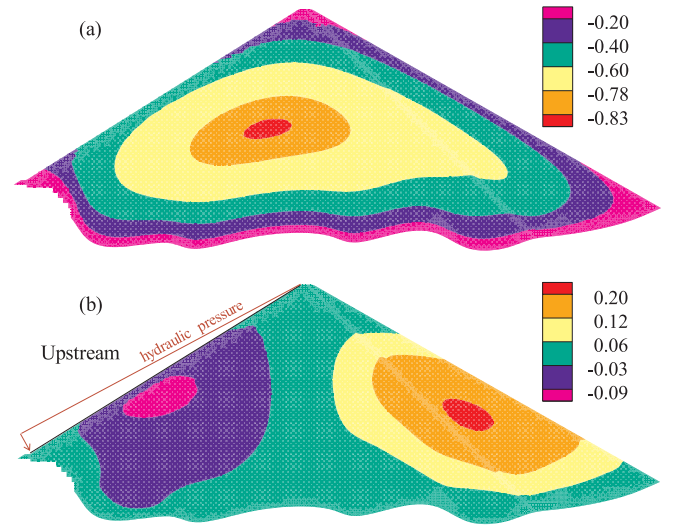


Fig. 5-8. Displacements of the representative cross-section after impoundment (units: m) in the (a) y-direction and (b) x-direction.

the representative two-dimensional cross-section after impoundment. The vertical settlement near the half dam height is quite high, and the maximum displacement is 0.83 m, representing 0.34% of the dam height. Meanwhile, the upstream dam movement is partly restricted due to hydraulic pressure, resulting in the maximum response along the

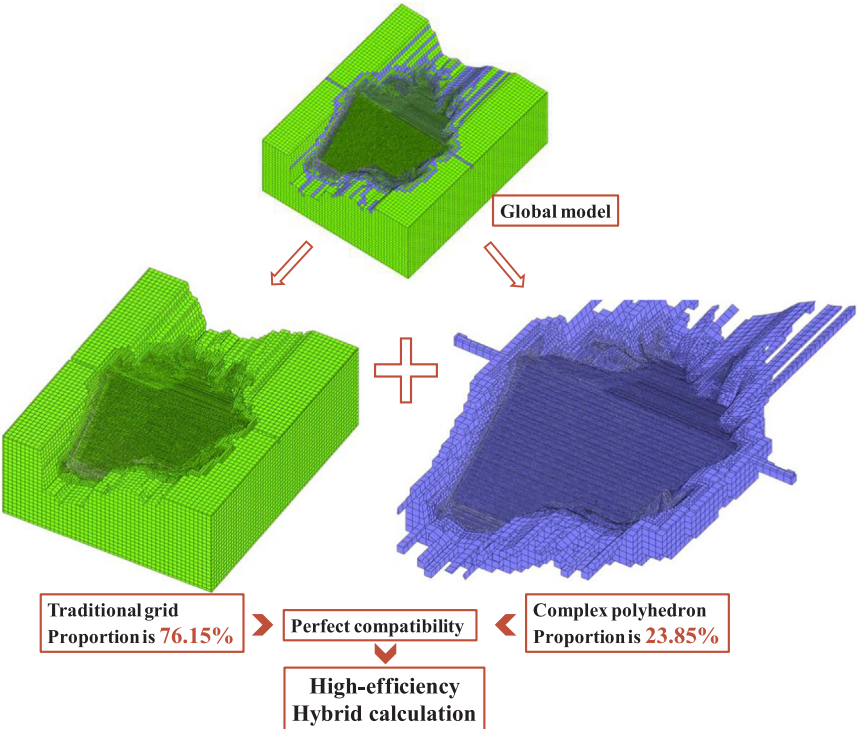


Fig. 5-7. Distribution of grid types in the global CFRD model.

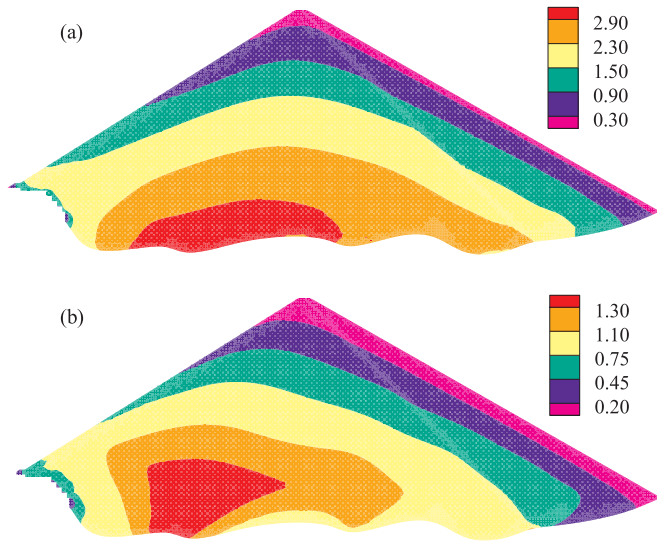


Fig. 5-9. Principal stresses of the representative cross-section after impoundment (units: MPa): (a) major principal stress and (b) minor principal stress.

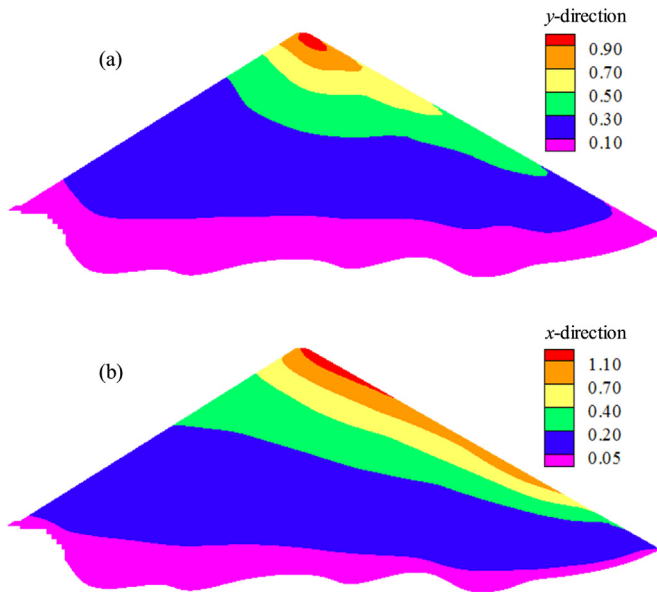


Fig. 5-10. Displacements of the representative cross-section during earthquake ground motion (units: m) in the (a) x-direction and (b) y-direction.

x-direction in the dam body located downstream.

The maximum stress should appear at the bottom of the dam, which is revealed in Fig. 5-9. The maximum major principal stress is 2.9 MPa, and the minor principal stress is 1.3 MPa.

5.5.2. Dynamic results

5.5.2.1. Dam body. Then, the nephogram of the CFRD generated in response to earthquake ground motion is discussed to validate the dynamic analysis. The final results of the identical cross-section are displayed in Figs. 5-10 and 5-11, which exhibit the dynamic displacement and total residual deformation after the seismic ground motion.

As can be seen in Fig. 5-11, the maximum seismic subsidence occurring on the dam crest is 0.90 m, which represents 0.364% of the height of the dam. It is vital to consider this degree of subsidence when designing a dam to guarantee its proper functioning after an earthquake.

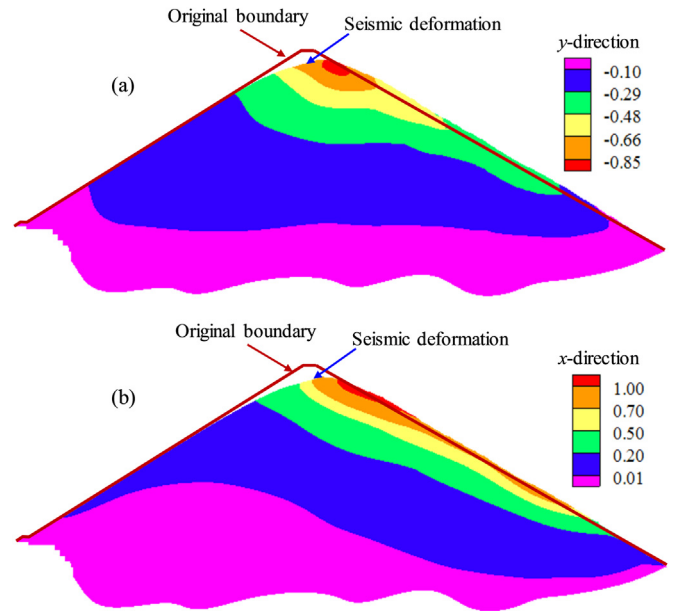


Fig. 5-11. Total deformation of the representative cross-section after earthquake ground motion: (a) x-direction and (b) y-direction (20x magnification).

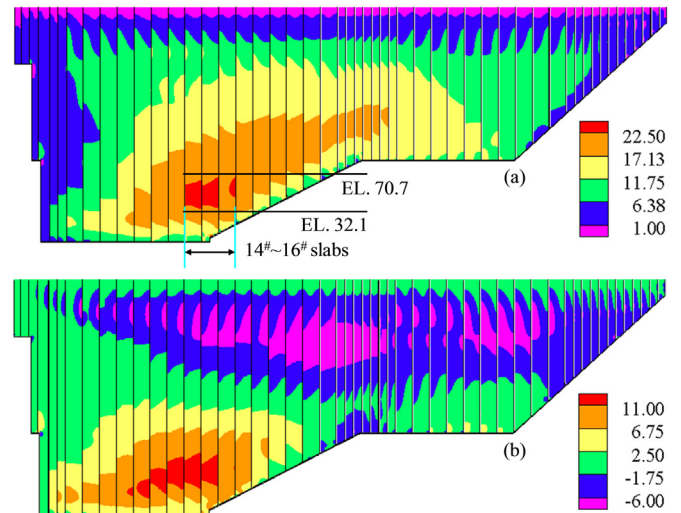


Fig. 5-12. Contour lines of stress along the slope direction in the slab during the earthquake: (a) major stress along the slope direction, (b) minor stress along the slope direction (compressive stress is positive, unit: MPa).

5.5.2.2. Concrete face slabs. We extract the maximum response at each time of input motion during an earthquake, which represents its most dangerous state. Fig. 5-12 displays the predicted stress developments during seismic loading in the slab elements (where the compressive stress is positive). The scope of maximum concrete stress along the slope direction induced in the #14~#16 slabs (from elevations of 32.1–70.7 m) is marked in the contour distribution. As the face slab is confined between two abutments, the out-of-plane motion of the abutments in the slope direction can exert relatively large horizontal forces on the face slab. The scattered ground input motion has increasing effects on both compressive and tensile forces due to the seismic subsidence motions of the abutments, ultimately creating a maximum compressive stress of 22.50 MPa and a tensile force of 6.0 MPa distributed near the middle-upper part of the slabs.

When the slabs slide down along the slope direction, a component along the axial direction of the dam causes the slabs to increasingly squeeze each other, leading to a considerable crushing stress in the

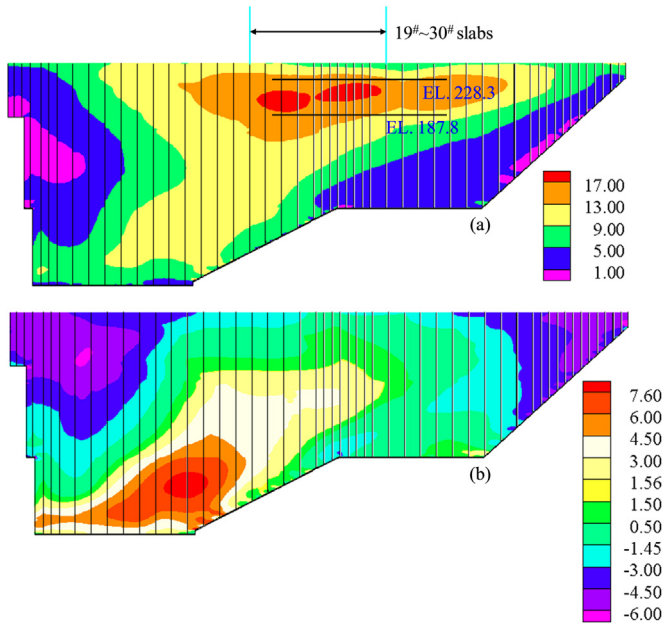


Fig. 5-13. Contour lines of stress along the axial direction of the dam in the slab after the earthquake: (a) major stress along the axial direction of the dam, (b) minor stress along the axial direction of the dam (compressive stress is positive, unit: MPa).

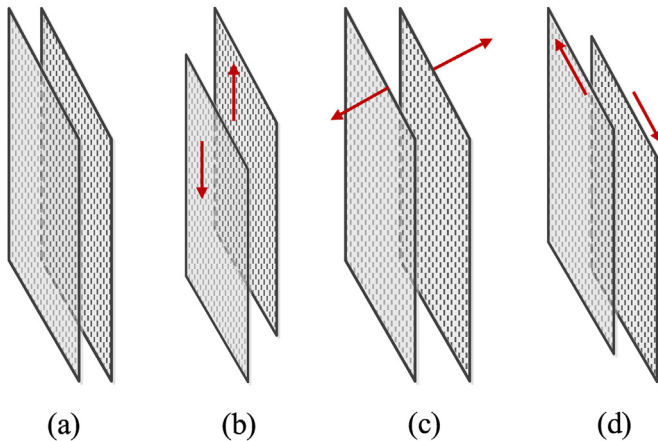


Fig. 5-14. Definition of the types of joint movement: (a) initial situation, (b) shear parallel to the joint, (c) opening normal to the joint, (d) movement normal to the concrete face slab.

Table 5-5

Movements of the joints between slabs (unit: cm).

Joint type	Shear parallel	Opening normal	Movement normal
vertical joint	1.76	2.01	0.81
peripheral joint	3.31	2.57	2.43

#19–#30 slabs at elevations of 187.8–228.3 m (see Fig. 5-13). The maximum value of this stress can be evaluated as 17.0 MPa. Meanwhile, the tensile stress along the dam axis is more than 3.0 MPa, which is greater than the tensile strength of the concrete ($f_t = 1.57$ MPa) and is mainly distributed near the side slopes. In summary, the numerical simulation of the slab stresses agreed well with the observed slab stresses presented in the literature [3,7,48,54].

Obvious discontinuous distributions can be observed between the slabs, which are divided by the vertical joints. These discontinuities are ascribed to the use of refined grids, as a coarse mesh would yield

average stress values. Some interesting phenomena may be missed during the equalization process.

5.5.2.3. Movement of joints. The movements of the vertical and peripheral joints are vital for slab stability, in addition to inducing forces in the face slab. Generally, three types of joint movement, namely, shear parallel to the joint, opening normal to the joint, and movement normal to the concrete slab, are expected in vertical joints (as shown in Fig. 5-14).

Table 5-5 lists the maximum joint displacements. First, the shear parallel component is generated because of the earthquake-generated subsidence of the slabs and dam body. Second, the opening normal component is computed after the earthquake. As the joint opening is dependent upon the out-of-phase lateral movements of the abutments, the maximum opening appears near the side slopes where the tensile stress is observed. The normal movement of joints is due to the flexural deformation of the slab panels resulting from the repeated uplift and downfall of the slab on the dam body.

Overall, the general distribution pattern of this simulation is reasonable and agrees well with those reported by others [3,7,48,54], which demonstrates that the proposed method performs commendably.

6. Conclusions

A multistage concurrent cross-scale mesh refinement method based on a hybrid octree method is presented in this paper to model complicated large-scale projects in three dimensions. In order to automatically match the produced grids, a versatile polygon interface element and viscoelasticity artificial boundary are subsequently explored based on the mean-value polygon technique. Additionally, a combined computation scheme coupling finite element analysis and the scaled boundary polyhedron finite element method is recommended to optimize the solution procedure by taking full advantage of their inherent strengths.

Using the proposed methods, an alternative efficient meticulous analysis system for massive complicated geotechnical engineering applications is established:

- (1) A concurrently meticulous cross-scale mesh generation of an intricate, high concrete-faced rockfill dam can be accomplished automatically in a few minutes, in contrast to a traditional coupled cross-scale mesh (i.e., using the multigrid method, substructure technique and master-slave method). Using this method negates the relative time-consuming discretization pattern and significantly accelerates the modelling processes of complicated geometries.
- (2) The interactions between a concrete face, rockfill and foundation can be captured with the help of a developed polygon interface element. Additionally, a more reasonable method of seismic response analysis is realized through the implementation of an octree viscoelasticity artificial boundary, which remedies the deficiency that a traditional model with a rigid boundary cannot consider the influence of the radiation damping of an infinite foundation and that of the travelling wave effect on the dynamic response and stabilization of the rockfill dam.
- (3) A benefit of the cross-scale method is that nearly 90% of regions are occupied by coarse grids without compromising computational accuracy. Additionally, a combined perfectly compatible calculation strategy is adopted where the minority polyhedrons are handled using SBFEM and the remaining majority hexahedrons are calculated via the traditional isoparametric element, in which approximately 27 h are needed to complete an elasto-plastic refined simulation of a 30-s seismic duration on a small workstation (2.40 GHz CPU, 44 cores).

The primary issue facing the refined analysis of extremely complicated large-scale projects is the model generation strategy and solving

efficiency. Solutions of these problems would represent important advances in eliminating the engineering design-to-analysis bottleneck. For a particularly promising technology, the octree-based scaled boundary polyhedron finite element is expected to be thoroughly generalized to a wider variety of analytical applications, such as enormous subterranean structures, nuclear plants and architectural and aviation structures.

Acknowledgements

This work was supported by National Key R&D Program of China (2017YFC0404900) and the National Natural Science Foundation of China (Grant Nos. 51779034, 51678113).

References

- [1] Bazilevs Y, Calo VM, Cottrell JA, et al. Isogeometric analysis using T-splines. *Comput Methods Appl Mech Eng* 2010;199(5–8):229–63.
- [2] Lian H, Kerfriden P, Bordas SPA. Shape optimization directly from CAD: an isogeometric boundary element approach using T-splines. *Comput Methods Appl Mech Eng* 2017;317:1–41.
- [3] Khalid S, Singh B, Nayak GC, et al. Nonlinear analysis of concrete face rockfill dam. *J Geotech Eng* 1990;116(5):822–37.
- [4] Chen Q, Zhang LM. Three-dimensional analysis of water infiltration into the Gouhou rockfill dam using saturated unsaturated seepage theory. *Can Geotech J* 2006;43(5):449–61.
- [5] Liu H, Zou D. Associated generalized plasticity framework for modeling gravelly soils considering particle breakage. *J Eng Mech* 2012;139(5):606–15.
- [6] Liu J, Liu F, Kong X, et al. Large-scale shaking table model tests of aseismic measures for concrete faced rock-fill dams. *Soil Dyn Earthq Eng* 2014;61:152–63.
- [7] Zou D, Xu B, Kong X, et al. Numerical simulation of the seismic response of the Zipingpu concrete face rockfill dam during the Wenchuan earthquake based on a generalized plasticity model. *Comput Geotech* 2013;49:111–22.
- [8] Xu B, Zhou Y, Zou D. Numerical simulation on slabs dislocation of Zipingpu concrete faced rockfill dam during the Wenchuan earthquake based on a generalized plasticity model. *Sci World J* 2014;2014.
- [9] Xu B, Zou D, Kong X, et al. Dynamic damage evaluation on the slabs of the concrete faced rockfill dam with the plastic-damage model. *Comput Geotech* 2015;65:258–65.
- [10] Qu Y, Zou D, Kong X, et al. A novel interface element with asymmetric nodes and its application on concrete-faced rockfill dam. *Comput Geotech* 2017;85:103–16.
- [11] Olshanskii MA, Terekhov KM, Vassilevski YV. An octree-based solver for the incompressible Navier-Stokes equations with enhanced stability and low dissipation. *Comput Fluids* 2013;84:231–46.
- [12] Popinet S. An accurate adaptive solver for surface-tension-driven interfacial flows. *J Comput Phys* 2009;228(16):5838–66.
- [13] Fuster D, Bagné A, Boeck T, et al. Simulation of primary atomization with an octree adaptive mesh refinement and VOF method. *Int J Multiph Flow* 2009;35(6):550–65.
- [14] Korkut B, Li Z, Levin DA. 3-D simulation of ion thruster plumes using octree adaptive mesh refinement. *IEEE Trans Plasma Sci* 2015;43(5):1706–21.
- [15] Zhu YZ. Studies on strain localization, ductile fracture and damage in structural metals; 2017.
- [16] Bishop JE. A displacement-based finite element formulation for general polyhedra using harmonic shape functions. *Int J Numer Methods Eng* 2014;97(1):1–31.
- [17] Wolf JP, Song CM. Finite-element modelling of unbounded media. Chichester: Wiley; 1996.
- [18] Beskos DE. Boundary element methods in dynamic analysis. *Appl Mech Rev* 1987;40(1):1–23.
- [19] Beskos DE, Maier GE. Boundary element advances in solid mechanics. Springer; 2014.
- [20] Liu J, Lin G. A scaled boundary finite element method applied to electrostatic problems. *Eng Anal Bound Elem* 2012;36(12):1721–32.
- [21] Liu J, Zhang PC, Lin G, et al. High order solutions for the magneto-electro-elastic plate with non-uniform materials. *Int J Mech Sci* 2016;115:532–51.
- [22] Ooi ET, Song C, Tin-Loi F. A scaled boundary polygon formulation for elasto-plastic analyses. *Comput Methods Appl Mech Eng* 2014;268:905–37.
- [23] Chen K, Zou D, Kong X, et al. A novel nonlinear solution for the polygon scaled boundary finite element method and its application to geotechnical structures. *Comput Geotech* 2017;82:201–10.
- [24] Chen K, Zou D, Kong X. A nonlinear approach for the three-dimensional polyhedron scaled boundary finite element method and its verification using Koyna gravity dam. *Soil Dyn Earthq Eng* 2017;96:1–12.
- [25] Goswami S, Becker W. Computation of 3-D stress singularities for multiple cracks and crack intersections by the scaled boundary finite element method. *Int J Fract* 2012;175(1):13–25.
- [26] Ooi ET, Shi MG, Song CM, et al. Dynamic crack propagation simulation with scaled boundary polygon elements and automatic remeshing technique. *Eng Fract Mech* 2013;106:1–21.
- [27] Ooi ET, Natarajan S, Song C, et al. Dynamic fracture simulations using the scaled boundary finite element method on hybrid polygon quadtree meshes. *Int J Impact Eng* 2016;90:154–64.
- [28] Saputra AA, Birk C, Song C. Computation of three-dimensional fracture parameters at interface cracks and notches by the scaled boundary finite element method. *Eng Fract Mech* 2015;148:213–42.
- [29] Lu S, Liu J, Lin G, et al. Time-domain analyses of the layered soil by the modified scaled boundary finite element method. *Struct Eng Mech* 2015;55(5):1055–86.
- [30] Birk C, Behnke R. A modified scaled boundary finite element method for three-dimensional dynamic soil-structure interaction in layered soil. *Int J Numer Methods Eng* 2012;89(3):371–402.
- [31] Lu S, Liu J, Lin G, et al. Modified scaled boundary finite element analysis of 3D steady-state heat conduction in anisotropic layered media. *Int J Heat Mass Transf* 2017;108:2462–71.
- [32] Lin G, Liu J, Li J, et al. A scaled boundary finite element approach for sloshing analysis of liquid storage tanks. *Eng Anal Bound Elem* 2015;56:70–80.
- [33] Xu H, Zou D, Kong X, et al. A nonlinear analysis of dynamic interactions of CFRD-compressible reservoir system based on FEM-SBFEM. *Soil Dyn Earthq Eng* 2018;112:24–34.
- [34] Liu J, Lin G, Li J. Short-crested waves interaction with a concentric cylindrical structure with double-layered perforated walls. *Ocean Eng* 2012;40:76–90.
- [35] Gravenkamp H, Saputra AA, Song C, et al. Efficient wave propagation simulation on quadtree meshes using SBFEM with reduced modal basis. *Int J Numer Methods Eng* 2017;110(12):1119–41.
- [36] Chen D, Birk C, Song C, et al. A high-order approach for modelling transient wave propagation problems using the scaled boundary finite element method. *Int J Numer Methods Eng* 2014;97(13):937–59.
- [37] Li P, Liu J, Lin G, et al. A NURBS-based scaled boundary finite element method for the analysis of heat conduction problems with heat fluxes and temperatures on side-faces. *Int J Heat Mass Transf* 2017;113:764–79.
- [38] Xu H, Zou D, Kong X, et al. Study on the effects of hydrodynamic pressure on the dynamic stresses in slabs of high CFRD based on the scaled boundary finite-element method. *Soil Dyn Earthq Eng* 2016;88:223–36.
- [39] Xu H, Zou D, Kong X, et al. Error study of Westergaard's approximation in seismic analysis of high concrete-faced rockfill dams based on SBFEM. *Soil Dyn Earthq Eng* 2017;94:88–91.
- [40] Zou DG, Teng XW, Chen K, et al. An extended polygon scaled boundary finite element method for the nonlinear dynamic analysis of saturated soil. *Eng Anal Bound Elem* 2018;91:150–61.
- [41] Liu Y, Saputra AA, Wang J, et al. Automatic polyhedral mesh generation and scaled boundary finite element analysis of STL models. *Comput Methods Appl Mech Eng* 2017;313:106–32.
- [42] Saputra A, Talebi H, Tran D, et al. Automatic image-based stress analysis by the scaled boundary finite element method. *Int J Numer Methods Eng* 2017;109(5):697–738.
- [43] Zou D, Chen K, Kong X, et al. An enhanced octree polyhedral scaled boundary finite element method and its applications in structure analysis. *Eng Anal Bound Elem* 2017;84:87–107.
- [44] Floater MS, Kós G, Reimers M. Mean value coordinates in 3D. *Comput Aided Geom Des* 2005;22(7):623–31.
- [45] Sukumar N, Tabarraei A. Conforming polygon finite elements. *Int J Numer Methods Eng* 2004;61:2045–66.
- [46] Samadhiya NK, Viladkar MN, Al-Obaydi MA. Three-dimensional joint/interface element for rough undulating major discontinuities in rock masses. *Int J Geomech* 2008;8(6):327–35.
- [47] Liu H, Ling HI. Constitutive description of interface behavior including cyclic loading and particle breakage within the framework of critical state soil mechanics. *Int J Numer Anal Methods Geomech* 2008;32(12):1495–514.
- [48] Kong X, Zhou Y, Zou D, et al. Numerical analysis of dislocations of the face slabs of the Zipingpu Concrete Faced Rockfill Dam during the Wenchuan earthquake. *Earthq Eng Eng Vib* 2011;10(4):581–9.
- [49] Liu J, Zou D, Kong X. A three-dimensional state-dependent model of soil-structure interface for monotonic and cyclic loadings. *Comput Geotech* 2014;61:166–77.
- [50] Yu Y, Bathurst RJ. Influence of selection of soil and interface properties on numerical results of two soil-geosynthetic interaction problems. *Int J Geomech* 2016;17(6):04016136.
- [51] Zhang G, Zhang JM. Unified modeling of monotonic and cyclic behavior of interface between structure and gravelly soil. *Soils Found* 2008;48(2):231–45.
- [52] Liu J, Kong X, Zou D. Effects of interface models on deformation of interface between slab and cushion layer and slab stress of concrete faced rock fill dam. *J Geotech Eng* 2015;37(4):700–10.
- [53] Wong HL. Effects of surface topography on the diffraction of P, SV and Rayleigh waves. *Bull Seismol Soc Am* 1982;72(4):1167–83.
- [54] Xu B, Zou D, Liu H. Three-dimensional simulation of the construction process of the Zipingpu concrete face rockfill dam based on a generalized plasticity model. *Comput Geotech* 2012;43:143–54.